

## Expanded North Pacific Subtropical Gyre and heterodyne expression during the mid-Pleistocene

S. P. Taylor<sup>1\*</sup>, M. O. Patterson<sup>1</sup>, A. R. Lam<sup>1</sup>, H. Jones<sup>1</sup>, S. C. Woodard<sup>2</sup>, M. H. Habicht<sup>3</sup>, E.K. Thomas<sup>4</sup> and G. Grant<sup>5</sup>

<sup>1</sup> Binghamton University, Department of Geology and Environmental Studies, Binghamton, New York 13902

<sup>2</sup> Global Aquatic Research LLC, Sodus, New York 14551

<sup>3</sup> The University of Michigan Biological Station, Ann Arbor, MI 48109-1085

<sup>4</sup> University of Buffalo, Department of Geology, Buffalo, NY 14260-1350

<sup>5</sup> GNS Science, Lower Hutt, New Zealand

Corresponding author: Shawn Taylor ([staylor5@binghamton.edu](mailto:staylor5@binghamton.edu))

### Key Points:

- Non-linear influences on Northwest Pacific oceanic circulation during the 41-k.y. world
- Pronounced periods of warmth during MIS 29–25, 15, 11–9 under a colder climate regime
- Changes in North Pacific Subtropical Gyre correspond to extreme Arctic warming events

This is the author manuscript accepted for publication and has undergone full peer review but has not been through the copyediting, typesetting, pagination and proofreading process, which may lead to differences between this version and the [Version of Record](#). Please cite this article as [doi: 10.1029/2021PA004395](https://doi.org/10.1029/2021PA004395).

This article is protected by copyright. All rights reserved.

## Abstract

The Kuroshio Current (KC) and Kuroshio Current Extension (KCE) form a western boundary current as part of the North Pacific Subtropical Gyre. This current plays an important role in regulating weather and climate dynamics in the Northern Hemisphere in part by controlling the delivery of moisture to the lower atmosphere. Previous studies indicate the KCE responded dynamically across glacial and interglacial periods throughout the Pliocene-Pleistocene. However, the response of the KCE during Pleistocene super interglacials has not been examined in detail. We present a ~2.2 Ma record of X-ray fluorescence elemental data from Ocean Drilling Program Hole 1207A and employ hierarchical clustering techniques to demonstrate paleoenvironmental changes around the KCE. Time-frequency analysis identifies significant heterodyne frequencies, which suggests there were non-linear interactions between high and low-latitude climate regulating expansion and contraction of the North Pacific Subtropical Gyre prior to the onset of the Mid-Pleistocene Climate Transition (MPT). We observe two periods of elevated  $\ln Ca/Ti$ , which may represent sustained warmth with northward migrations of the KCE in the northwestern Pacific. These intervals correspond to Marine Isotope Stages 29–25, 15, and 11–9 and occur around recent climatic transitions, the MPT and Mid-Brunhes Event. Northward expansion of the subtropical gyre during these exceptionally warm interglacials would have delivered more heat and moisture to the high latitudes of the northwest Pacific. Furthermore, enhanced evaporation from the warm KCE vented to the lower atmosphere may have preconditioned the Northern Hemisphere for ice volume growth during two of the most recent periods of climate transition.

## 1 Introduction and Background

Robust predictions to assess the consequences of future warming for Earth's climate system require a geological perspective in order to examine the causal mechanisms and full range of environmental change possible over various warming scenarios. Mid- to high-latitude paleoclimate records are particularly important as these regions play a major role in regulating

the global climate system through feedbacks involving the ocean, atmosphere, cryosphere, and terrestrial processes. Notably, these mid-latitude regions of the world ocean are characterized by western boundary currents as part of subtropical and subpolar gyre systems. Western boundary currents have large influences on storm tracks and precipitation patterns and are warming 2–3 times faster than the average ocean sea surface temperature (Hu et al., 2015). In the Northern Hemisphere, the Kuroshio Current (KC) and the Kuroshio Current Extension (KCE) are important components of the North Pacific Western Boundary current system as they modulate weather and climate patterns over the Northern Hemisphere (Hu et al., 2015). Thus, it is imperative to understand how the Kuroshio Current system will behave due to increased anthropogenic warming under a range of warming scenarios using an array of methods. One of the most advantageous methods to observe long-term climate trends of the current is through the use of the sedimentary record (e.g., Venti and Billups, 2013; Abell et al., 2021; Lam et al., 2021).

The KC is the wind-driven northwest Pacific subtropical western boundary current, part of the North Pacific Subtropical Gyre (Andres et al., 2015). The KC is sourced from the westward-flowing North Equatorial Current. From the western equatorial Pacific, the current flows north, past the Izu Ridge, where it separates from the Japan coast around 36°N, 141°E. Here, it flows eastward into the Pacific Ocean as the KCE (Imawaki et al., 2013; Fig. 1). The KCE meets the southward-flowing Oyashio Current off the coast of Japan, which forms the Kuroshio-Oyashio Transition Zone. This region is characterized by the mixing of warm waters transported north by the KCE and cool nutrient-rich subarctic surface waters transported south by the Oyashio Current (Sakurai, 2007; Long et al., 2019).

The KCE plays an important role in regulating weather and climate dynamics in the Northern Hemisphere (Latif and Barnett, 1994; Miller et al., 1998; Deser et al., 1999; Kwon et al., 2010; Hu et al., 2015) as it is the primary mechanism in transporting heat and moisture poleward in the western Pacific (da Silva et al., 1994). Heat and moisture from the KCE vent to the lower atmosphere which provides the necessary means to support storms and influence storm tracks in the North Pacific (Nakamura et al., 2004). Through changes in the current's position and intensity, and decadal changes between its stable (less variable flow path) and unstable (more variable flow path) states, the KCE can influence the stability and pressure gradient within atmospheric boundary layers and alter basin-scale wind patterns (Frankignoul and Sennéchaël, 2007; Kwon et al., 2010).

Since the KCE exerts a strong influence on the weather and climate patterns of the North Pacific, it remains critical to understand how the current will behave beyond decadal timescales in response to increased anthropogenic warming. Modeling studies of the KCE indicate the current will continue to warm, shift its latitudinal position northward, and increase its transport capacity (e.g., Sakamoto et al., 2005; Zhang et al., 2017; Nishikawa et al., 2020). However, a large unknown regarding future climate change is the degree to which the KCE will warm and affect climate system dynamics of the Northern Hemisphere as global mean temperatures reach or exceed a 2°C warming compared to pre-industrial values (Bindoff et al., 2019).

Studies using paleontological and sedimentological proxies indicate the Kuroshio Current region responded dynamically across glacial and interglacial periods during the Pleistocene (e.g., Kitamura et al., 1999; Kawahata and Ohshima, 2002; Kawahata and Ohshima, 2004; Yamamoto et al., 2005; Kitamura and Kimoto, 2006; Hoiles et al., 2012). During the Last Glacial Maximum

(~20 ka), the KC shifted equatorward and eastward (Ahagon et al., 1993; Jian et al., 1998; Ujiie and Ujiie, 1999), with a subsequent migration back to its pre-glacial maximum position around 7.5–6.0 ka (Jian et al., 1998). During the Holocene, the mean latitude of the KCE varied in response to millennial/sub-orbital scale (~1500-yr) forcing associated with changes in sea surface temperature and North Atlantic thermohaline circulation (Jian et al., 2000; Isono et al., 2009). The Pleistocene behavior of the KCE is less well-known compared to its Holocene behavior, but studies do indicate that in the last 600 ka the KCE underwent large changes in its velocity and latitudinal location in response to middle Pleistocene climate instability (Ito and Horikawa, 2000; Kawahata and Ohshima, 2002; Yamane, 2003; Ujiie, 2003). During Pleistocene interglacial periods, the KC likely shifted eastward compared to glacial periods and decelerated in response to rising sea levels (Chen et al., 1992). Thus, these studies demonstrate that the Kuroshio Current region responded sensitively to some of the most recent glacial and interglacial cycles, by shifting both position and velocity.

Over the past 2 million years of Earth's history, the climate system underwent dramatic transitions in both the pacing (during the Mid-Pleistocene Climate Transition [MPT] 1.25–0.80 Ma) and amplitude (during the Mid-Brunhes Event [MBE] at ~0.43 Ma) variability of glacial to interglacial periods (e.g., Ahn et al., 2017). Additionally, the eastern terrestrial Arctic experienced episodes of extreme warming referred to as super interglacials (i.e., Marine Isotope Stages [MIS] 11, 21, 27, 29) (Melles et al., 2012; Lindberg et al., 2022). These past periods of transition and warming provide partial analogs to investigate how the KCE may respond to times of climate reorganization and elevated global mean temperatures that are projected for the coming decades (IPCC, 2021). Although the orbital parameters during super interglacial periods were different from today, paleoenvironmental reconstructions suggest global mean temperatures were 1–2°C higher than pre-industrial values, at least during MIS 11 (Lang and Wolff, 2011) and thus may provide insights into past sensitivities in surface oceanic circulation that are expected with projected warming in the future (IPCC, 2021).

Here we investigate the behavior of the KCE across Pleistocene super interglacials, the MPT and the MBE, in order to examine the role and feedbacks the KCE plays in the climate system during some of the most well-studied and accessible analogs of extreme warmth and transition. In this study, we use inorganic geochemical proxies to assess changes in the latitudinal position of the KCE and use robust statistical techniques to identify orbital variability within our record. We place our results in the context of existing data sets recovered from Asia, the Pacific Ocean, and Northern America. We hypothesize that non-linear responses of KCE circulation regime to orbital forcing may have led to prolonged periods of enhanced warmth and moisture delivery to the North Pacific. These ocean-atmospheric dynamic responses to orbital forcing could have provided greater moisture to regions of higher elevation and latitude along western North America, thus promoting ice volume growth for the last ~2.2 Ma.

## 2 Materials and Methods

High-resolution non-destructive geochemical analysis used in combination with visual core description and shipboard physical property data provides a wealth of knowledge concerning the depositional processes in marine sediment cores that are related to past environmental change. Unsupervised (without model training and set outcome) statistical techniques are useful to summarize physical properties and XRF data, which reflect downhole changes in lithofacies occurring at centimeter to meter scales (Penkrot et al., 2018). We adopt a



similar methodology as described by Penkrot et al. (2018), but include additional techniques used previously for open marine records on XRF core scanning data (e.g., Bahr et al., 2014) in order to examine the stratigraphic distribution of lithofacies change reflected at Ocean Drilling Program (ODP) Hole 1207A for the past ~2.2 Ma.

### 2.1 Lithostratigraphy of ODP Hole 1207A

ODP Leg 198 drilled eight sites on Shatsky Rise in the northwest Pacific in 2001 (Bralower et al., 2002). Site 1207 was drilled from the northern high (Shirshov Massif; Sager et al., 2013) of Shatsky Rise and contains a near continuous late-Neogene to Quaternary sedimentary record (Bralower et al., 2002). Currently, Site 1207 is located below the transition zone between subtropical waters to the south, and subarctic waters brought equatorward by the Oyashio Current (Fig. 1). Given its position, the site is ideally located to monitor changes in water masses passing over the site in response to abiotic factors during critical climate events of the geologic past. For example, a southward shift of the Aleutian Low (low-pressure system) and Oyashio Current would displace subarctic waters southward during colder-than-present intervals of the Pleistocene, thus making it likely Site 1207 was positioned below the southern edge of the subarctic front. During warmer-than-present times, expansion of the North Pacific Subtropical Gyre would extend beyond Site 1207 (e.g., Fedorov et al., 2013; Ford et al., 2016; Lam and Leckie, 2020a; Lam et al., 2021).

A complete Pleistocene (2.58–0.01Ma) record was recovered from Hole 1207A (~103% core recovery) with no indication of major drilling disturbances (Bralower et al., 2002; Evans et al., 2005). The upper 30 meters (~2.16 Ma to recent) is defined by lithostratigraphic unit 1A, consisting of decimeter-scale interbeds of darker clayey nannofossil ooze (calcareous nannofossil dominant,  $\geq 25\%$  clay) and lighter nannofossil ooze with clay (calcareous nannofossil dominant,  $<25\%$  clay) layers (Bralower et al., 2002; Fig. 2a). Contacts between interbeds are typically gradational from clayey nannofossil ooze (dark) to nannofossil ooze with clay (light), with sharp upper contacts (i.e. light to dark). Shipboard color reflectance data demonstrates the cyclical nature of these sediments with the greatest variability during the early to mid-Pleistocene (~30–19 mbsf; Bralower et al., 2002). These lithological changes most likely reflect variability in surface ocean circulation as a result of expansion and contraction of the subtropical gyre (Bralower et al., 2002; Lam and Leckie, 2020a) rather than dissolution (Lam and Leckie, 2020a). While it has been argued that this frontal system is stabilized via the bathymetric high of Shatsky Rise (e.g., Jacobi and Hayes, 1989; Venti et al., 2013;), initial results from Leg 198 (Bralower et al., 2002) and subsequent work (Lam and Leckie, 2020a; Lam et al., 2020; Lam et al., 2021) demonstrate that through the Neogene and Quaternary, latitudinal shifts of the KCE and water masses may have been much more significant compared to those that have occurred within the last 600 kyr (e.g., Kawahata and Ohshima, 2002; Yamane, 2003; Ujiie, 2003).

### 2.2 XRF Core Scanning

A 4th Gen Avaatech Core Scanner was used for XRF core scanning of the sediments from Hole 1207A at the International Ocean Discovery Program's (IODP) Gulf Coast Repository, Texas A&M University. Measurements were taken at an average spacing of 2 cm downcore over a 1 cm<sup>2</sup> spot size, corresponding to a median temporal resolution of 2 kyrs (Lam and Leckie, 2020b). Scanning took place on archive halves at three excitation conditions (10, 30,

and 50 kVp) with the split core surface covered in 4-micron thick SPEX Certi-Prep Ultralene 1 film to prevent contamination of the XRF core scanning measurement detector. Pyrite laminae and blebs, voids, and cracks were avoided during scanning using visual inspection. The core scanner measured characteristic X-rays using Energy Dispersive Spectroscopy (EDS), in which photons of all energies are measured simultaneously, allowing for faster analyses at the expense of peak resolution (and therefore measurement accuracy and precision). Brightspec silicon drift detectors (SDD) were also used, which provide high-resolution peaks and high throughput (Bahr et al., 2014).

### 2.3 XRF data processing: statistical techniques for identifying lithofacies changes

The rapid, high resolution and non-destructive analytical capabilities of XRF core scanning are of particular importance as they permit a rapid estimation of lithological variability from marine sediment cores that reflect environmental change. These techniques provide semi-quantitative estimation of elemental composition through emission of secondary X-rays from sediment cores (Croudace and Rothwell, 2015). Previous studies have demonstrated that application of principle component analysis (PCA) on XRF core scanning data that contains a robust signal quality and environmental significance is useful in providing insight into physical and geochemical variability in a marine sediment core (e.g., Bahr et al., 2014; Jimenez-Espejo et al., 2020). Furthermore, Penkrot et al. (2018) demonstrated that unsupervised classification techniques of hierarchical cluster analysis on PCA results provide a useful way to determine lithofacies changes between mudstone and diamict (e.g., glaciomarine).

Raw data spectra were processed using the bAxil software using an ocean sediment model. The following elements are analyzed in this study given their robust signal and environmental significance: aluminum (Al), silica (Si), potassium (K), calcium (Ca), titanium (Ti), iron (Fe), bromine (Br), rubidium (Rb), strontium (Sr), zirconium (Zr), and barium (Ba). Data were treated with intention to remove any measurements resulting from poor contact, cracks, voids, sulfides, etc. Specifically, all data with a throughput of less than  $1.5 \times 10^5$  cps and/or greater than -1000 total counts per second of Ar were removed. All remaining data within observed tephra layers were removed (Bralower et al., 2002). Elemental data were then normalized in order to circumnavigate issues surrounding porosity, density and any water condensed below the film (e.g., Jansen et al., 1998; Tjallingij et al., 2007; Lyle et al., 2012; Bahr et al., 2014). The process of normalization followed that of Bahr et al. (2014). All normalized count data were then standardized by subtracting the mean and dividing by the standard deviation to observe downcore changes more easily in elemental distributions in order to assess signal quality. Prior to PCA, the normalized data were interpolated to the median sampling resolution of 2 cm and an isometric log-ratio (ilr) transformation was performed using the ‘*robCompositions*’ R package (Templ et al., 2008; Penkrot et al., 2018). Three principal components were identified that together explain over 90% of the variance of the XRF record (Table 1). These principal components were then used in hierarchical clustering analysis using Ward’s minimum linkage method in R using the “*hclust*” function (R Core Team, 2017; Penkrot et al., 2018; Taylor, 2021).

### 2.4 Time Series Analysis

The age model for this study was created using a combination of magnetostratigraphy (Lam and Leckie, 2020b) and calcareous nannofossil biostratigraphy from ODP Leg 198 (Bralower et al., 2002), with ages of calcareous nannofossil datums updated to those of Sutherland et al. (2019). In total, nine chrons and microfossil datums were used to constrain age to a depth of 30.00 mbsf (Table 3). This age model provides strong evidence for a continuous 2.2 Myr record at Hole 1207A with sedimentation rates (average of 1.45 cm/kyr) that resolve orbital-variability in a pelagic marine setting that is typical of Cenozoic benchmark studies with analogous sedimentation rates from the Atlantic Ocean sector (e.g., Zachos et al., 2004; Westerhold et al., 2012; Meyers, 2015). The well-resolved magnetostratigraphy and biostratigraphy at the site provides a robust age model independent of orbital tuning, whereby we can assess the imprint of orbital forcing in the framework of lithostratigraphy (e.g., Proistosescu et al., 2012; Patterson et al., 2014; Caballero-Gill et al., 2019; Reilly et al., 2021). Previous studies documenting the occurrence of planktic foraminifera species at this site and within the KCE system indicate that waters above Hole 1207A fluctuated from being in subtropical to subarctic through the late Neogene in response to tectonic and climate events (Lam and Leckie, 2020a, 2020b). Based on the occurrence of dissolution resistant vs. fragile species, the effects of dissolution were minimal for the Pliocene to Pleistocene sections of Hole 1207A (Lam and Leckie, 2020b). Thus, lithostratigraphic signatures from Hole 1207A have the potential to preserve a robust orbital signature of surface ocean changes.

Time series analyses in this study were performed using the R package ‘*astrochron*’ (Meyers, 2014). Data was re-sampled at a conservative median sampling resolution (2 kyr) using piecewise linear interpolation and was detrended from mean prior to analysis. An untuned age model (Lam and Leckie 2020a) was used to explore external forcing factors that may influence the expansion and contraction of the subtropical gyre system independent of ice volume changes as recorded in the global benthic foraminiferal oxygen isotope stack (e.g., Lisiecki and Raymo, 2005; Ahn et al., 2017; Reilly et al., 2021). Power spectral estimates were made using the robust locally weighted regression spectral background estimation (LOWSPEC), as this technique has been proven to produce substantially lower rates of false positive estimates compared to other methods (e.g., Mann and Lees, 1996). Furthermore, this technique also provides a better estimation of the overall detection of the combination of low and high frequencies associated with Milankovitch cycles (i.e., Mann and Lees, 1996; Meyers, 2012). We identify the frequencies that satisfy a 90% LOWSPEC confidence level and a 90% multitaper method harmonic F-test confidence level (Meyers, 2012). We then interpret our results in the context of the primary (cycle number is based on associated power) orbital frequencies associated with eccentricity (403.4 kyr = E4; 126.1 kyr = E2; 95.7 kyr = E1; and 54 kyr = E3), obliquity (53.7 kyr = O3; 41.1 kyr = O1; 28.9 kyr = O2), and precession (23.7 kyr = P2; 22.4 kyr = P3, and 19 kyr = P1) from 2164 ka using the Laskar et al. (2004) orbital solution (Fig. 3; Table 4), as our untuned age model provides this as a best estimate for overlap between the two records (i.e., orbital parameters and the Hole 1207A record).

Time-frequency analysis was carried out on pre-whitened stratigraphic data using autoregressive-1 (AR1 filter). Time-frequency MTM was employed with a 250-kyr window, and each window was linearly detrended from mean before analysis. Quantitative assessment of the evolution of power was determined by using the “intergrate power” function in the

'*astrochron*' R package. Cumulative power frequency analysis for eccentricity (0.001-0.15 1/kyr), obliquity (0.02-0.035), and precession (0.04-0.06) (Fig. 3; Taylor, 2021).

Heterodynes are time series power spectra peaks that do not fall at primary orbital frequencies (i.e. eccentricity, obliquity, and precession), but instead are combinations of two primary orbital frequencies. The presence of heterodynes indicates that multiple processes occurring at different primary orbital frequencies influence the record. Heterodynes have been well documented in late Pleistocene North Pacific regional climate records (eg. Wang et al., 2008; Thomas et al., 2014; Cai et al., 2015; Kathayat et al., 2016; Thomas et al., 2016). Heterodynes can be calculated by adding and subtracting primary orbital frequencies (frequency = 1/kyr) reflected in astronomical solutions (e.g., Rial and Anaclerio, 2000; Weedon, 2003; Clemens et al., 2010; Thomas et al., 2016). Given power spectra results discussed in section 3.3, heterodynes are examined at frequencies between 0.0133-0.2000 1/kyr for time-frequency analysis (Fig. 3; Taylor, 2021).

### 3 Results

#### 3.1 Characterization of Cluster lithologies

Here we identify stratigraphic changes in lithologies in a pelagic open marine setting using similar techniques as Penkrot et al., (2018). Our results indicate that cluster lithologies generally track shipboard visual core description and core photos at the meter-scale. However, at several depths throughout the core, cluster lithologies provide much greater detail and accuracy of composition and lithology at the sub-meter than the visual core descriptions do.

Prior to hierarchical cluster analysis, multivariate space was decreased by using three principal components (PC) that comprise 99.83% of the total variance (Table 1). Hierarchical cluster analysis produced two common clusters that compositionally matched lithologies identified by shipboard studies examining relative changes in lithofacies for Hole 1207A. The spatial relationship of the clusters is plotted downcore, creating a cluster lithology column (Fig. 2). Figure 2 shows downcore cluster lithology distributions and the normalized and standardized XRF elemental count data included in each cluster. Cluster 1 encompasses 65.75% of the record and is defined by positive values of standardized element counts that are expected for the shipboard classification of "clayey nannofossil ooze" lithology, as this cluster is enriched in elements that are typically indicative of terrigenous siliciclastic sources (i.e., Al, Si, K, Ti, Fe, Rb, Zr; Table 2). Cluster 2 encompasses 34.25% of the record and is defined by positive values of standardized elemental count data expected of "nannofossil ooze with clay" lithology, as this cluster is enriched in elements typically associated with marine carbonate biogenic oozes (i.e., Ca and Sr; Table 2). Decimeter-scale variability in cluster lithology is observed throughout the 30 m interval of sediments investigated (Fig. 2). The bottom ~11 m of the section (30–19 mbsf) is characterized by alternating nannofossil ooze with clay and clayey nannofossil ooze cluster lithologies at decimeter-scale beds. Thus, clear lithologic cycles are observed in this interval. Above ~19 mbsf this pattern transitions into a lithostratigraphy that is dominated by cluster 1 (Fig. 2). Cluster 1 (blue) makes up the bulk of the upper 19 m, except for several decimeter-scale cluster 2 (red) beds occurring between ~9 to 5 m and ~16.5 to 15 m.

Shipboard natural gamma radiation (NGR) and magnetic susceptibility (MS) agree well with positive values tracking with Cluster 1 throughout the core (Bralower et al., 2002; Fig. 4). Furthermore, XRF elements and ratios typically used for the determination of heavy minerals (e.g, Zr/Sr; Hodell et al., 2010), and carbonate-rich sediment (e.g, Ca/Ti; Arz et al., 1998; Bahr et al., 2005; Jaeschke et al., 2007; Bahr et al., 2008; Bourget et al., 2008; Kwiecien et al., 2009; Berg et al., 2010; Van Hoang et al., 2010; Tjallingii et al., 2010), accurately describe cluster lithologies (Figs. 4 and 5). We use log-ratios to account for a statistically more robust representation of element ratios that align with our cluster results (Weltje and Tjallingii 2008; Gruetzner and Higgins, 2010; Dunlea et al., 2020).

### 3.2 XRF proxies used for paleoenvironmental/paleoceanographic change

X-ray fluorescence counts and normalized log-ratios at ODP Hole 1207A indicate a high degree of variability through the study interval. We rely on two normalized log-ratios ( $\ln$  Ca/Ti and  $\ln$  Zr/Sr,) and four normalized elemental counts (Ca, Si Ti, and Zr) to interpret paleoceanographic changes associated with expansion and contraction of the North Pacific Subtropical Gyre and latitudinal shifts of the KCE (Fig. 4) Our results from the cluster analysis guided the determination of useful XRF ratios. Here we provide a review of how these elements and ratios have been used to interpret past paleoceanographic changes as it is relevant towards the interpretations in this study.

To further assess biogenic carbonate productivity at Hole 1207A, we plotted the normalized counts for Ca (Fig. 6). The Ca count data are also anticorrelated to Zr and Ti, further indicating that Ca, at this site, is not a terrigenous indicator but rather tracking biotic productivity. Additionally, Sr count data has statistically significant positive relationship with Ca throughout the record and previous works have demonstrated it as a carbonate-associated element (Bahr et al., 2014). To further display correlations between elements, we generated a correlation matrix following the ordination analysis workflow recommendations from Bialik et al., 2021 on all 11 elements (Fig. 7; Taylor, 2021). Correlation matrix results show strong anti-correlation between Ca and the siliciclastic sourced elements (i.e. Al, Si, K, Ti, Fe, Rb, and Zr).

The calcium to titanium (Ca/Ti) ratio is generally used to infer changes in the relative amounts of biogenic calcium carbonate to lithologic sediments in deep-sea cores (e.g., Piva et al., 2008; Ingram et al., 2010). Given the results of cluster analysis concerning the geochemical composition of lithofacies, we use the log ratio (i.e., Weltje and Tjallingii 2008; Gruetzner and Higgins, 2010) of Ca/Ti as a proxy for expansion and contraction of the subtropical gyre (Fig. 4), as warmer subtropical waters provide a relatively enhanced supply of biogenic carbonate to the seafloor compared to subarctic waters in this region (e.g., Dutkiewicz et al., 2015).

Zirconium (Zr) is generally most abundant in sedimentary zircons, a dense mineral that is commonly formed in igneous rocks, and due to its extreme hardness, can withstand weathering and transport processes (Liu et al., 2002; Chen et al., 2006; Westerhold et al, 2009; Liang et al., 2013; Wu et al., 2020). Thus, this mineral is often associated with coarser sediment size fractions in the deep marine system and has been used to identify volcanic ash layers (e.g., Westerhold et al., 2009). The ratio  $\ln$  Zr/Sr has been used to also infer ice-rafted debris in marine sediment cores (e.g., Hodell et al., 2010). In this study, we interpret the  $\ln$  Zr/Sr ratio to indicate heavy mineral deposition by winds (Martínez-García et al., 2010) but acknowledge ice-rafted debris



could be an additional source for the Late Quaternary (St. John & Krissek, 1999; McCarron et al., 2021). We use the counts of Zr along with titanium (Ti), which also occurs in terrestrial material to further investigate the influence of winds on the KCE.

Normalized and log-ratio Ca/Ti values, much like  $\ln$  Zr/Sr values, vary from 30 to ~19 mbsf. Within this interval, positive  $\ln$  Ca/Ti ratios correspond to negative  $\ln$  Zr/Sr values (Fig. 4). From ~19 to 16.5 mbsf,  $\ln$  Ca/Ti values become primarily negative, corresponding with the mainly positive  $\ln$  Zr/Sr values. From ~16.5 to 15 mbsf, the ratio then switches to mostly positive values, which again correspond to negative  $\ln$  Zr/Sr values. This switch to positive  $\ln$  Ca/Ti values and negative  $\ln$  Zr/Sr values occurs once more within a second interval from ~9 to 5 mbsf. The remainder of the upper ~15 m of the record,  $\ln$  Ca/Ti remains negative. Thus,  $\ln$  Ca/Ti functions as a relative estimate of subtropical vs. transitional/subarctic water masses passing over Hole 1207A.

Throughout the study interval,  $\ln$  Zr/Sr ratios increase and decrease cyclically from ~30 to 19 mbsf (Fig. 4). Beginning at ~19 mbsf,  $\ln$  Zr/Sr values become more positive, mostly associated with Cluster 1, a lithology characterized by clayey nannofossil ooze. There are two abrupt switches in values around ~16.5 and ~9 mbsf respectively, where values become mainly negative and indicate thick beds of nannofossil ooze with clay. From ~15 to ~9 mbsf and above 5 mbsf,  $\ln$  Zr/Sr ratios return to mainly positive values. Throughout the entire study interval, the counts of Zr and Ti seem to reflect cyclical change typical of glacial and interglacial cycles (Fig 6).

Silicon (Si) XRF data is commonly used to interpret terrigenous input to a region, or productivity related to the skeletal remains of siliceous plankton (Haug et al., 1999; Martínez-García et al., 2010). The Si count data mirror the Ti and Zr counts, indicating at Hole 1207A, Si is tracking terrigenous input (Fig. 6). However, Si content also includes biogenic opal, given the evidence from shipboard smear slide analysis (Bralower et al., 2002) and variability in biogenic opal mass accumulation rates in subarctic waters during the last 2 Ma (Haug et al., 1999). The co-variance of Si with Ti and Zr, may highlight the role of micronutrient delivery via windblown dust on primary productivity in the North Pacific (e.g., Haug et al., 1999; Martínez-García et al., 2010).

Our results from the cluster analysis demonstrate the legitimacy and usefulness of XRF elemental clustering in identifying lithological variability and identifying XRF proxies indicative of cyclical paleoenvironmental changes in open marine sediment records. This technique goes beyond the scope of shipboard visual core descriptions.

### 3.3. Frequency expression of lithofacies changes

The spectral characteristics typically associated with glacial-interglacial variability for the last ~2.2 Myrs typically demonstrate enhanced power associated with obliquity (41 kyr) prior to the MPT (1250 to 800 kyrs), whereas after the MPT (~800 ka), short-period eccentricity (126 and 95 kyr) contains more power (Fig. 3a-b; Ahn et al., 2017). Spectral characteristics of Hole 1207A stratigraphic changes in lithofacies spanning the last ~2.2 Ma exhibit significant variability associated with precession (24, 22 and 19 kyr), and obliquity (41 kyr) (Fig. 3).



However, the record does not exhibit the classic structure of primary frequencies associated with global ice volume and temperature changes (e.g., Ahn et al., 2017) correlating to short-period eccentricity (126 and 95 kyr) through the last 800,000 years of the studied interval (Fig. 3a-b, 3e-f). Notably, the spectra peaks surrounding the precession and obliquity associated periodicities appear to be stable (i.e., not offset or bifurcated) and the absence of the significant frequencies associated with the modulator of precession, long- and short-period eccentricity, is intriguing given the persistent strength of the precession signal throughout the record (Fig. 3f).

There is a large amount of spectral variance at frequencies not typically associated with orbitally-paced Quaternary paleoclimate records (e.g., 73, 62, and 50 kyr frequencies; Table 4). The spectral characteristics of these frequencies may represent distortions within the sedimentary record due to stratigraphic perturbations (e.g., hiatuses, compaction, sedimentation rate changes; Meyers et al., 2001; Meyers, 2019). Given that significant frequencies associated with periodicities at 73, 62, and 50 kyr are not characterized by a bifurcation of two new frequencies surrounding the 96 and 41 kyr periodic signals, we do not consider these frequencies to reflect the presence of a hiatus within our record (e.g., Meyers et al., 2001; Meyers 2019). This is further supported by relatively similar sedimentation rates throughout the record, the stability of the spectra peaks associated with precession (Fig. 3), and, at a coarser resolution, identification of all calcareous nannoplankton zones through the study interval (Bralower et al., 2002). While differential compaction and accumulation can alter the estimation of frequency content, particularly in alternating clay and carbonate-rich facies, this typically results in spectral leakage and the generation of harmonics of the primary frequency (Meyers et al., 2001). Harmonics of less power accompanying primary ~100 and 41-kyr periods are not observed within the spectra (e.g., Meyers et al., 2001; Fig. 3f). Furthermore, given that the CaCO<sub>3</sub> weight percent difference between lithofacies is typical of open marine sediments (<32%) (Meyers et al., 2001; Bralower et al., 2002), we consider that the influence of compaction and accumulation to be minimal, especially when considering that ~2 Myr is represented in the upper ~30 meters of the cored section at Hole 1207A, and porosity changes are minimal even in the upper 5 m of the core (Fig. 3). Variability in sedimentation rates would result in a shift of significant frequencies. However, both the precession and obliquity peaks are significant and stable, suggesting that variable sedimentation rates are not a cause of the 73, 62 and 50 kyr peaks in this record (Meyers et al., 2001; Meyers 2019).

Alternatively, such frequencies could be caused by sediment deposition changes that reflect expansion and contraction of the North Pacific Subtropical Gyre and KCE at periods that are non-linear in response to external forcing factors. In other words, lithofacies changes may be reflecting the impact of simultaneous forcing factors operating at different frequencies. Thus, the competing response between local insolation changes driving low-latitude climate variability dominated by precession, and changes in Northern Hemisphere high-latitude climate dominated by obliquity could result in heterodyne frequencies.

Time-frequency results demonstrate the covariance in power of heterodynes (75–50 kyr) and orbital frequencies associated with obliquity (41 kyr) and precession (~20 kyr) prior to ~800 ka in the Hole 1207A record. The power at precession and obliquity bands in the Hole 1207A lithostratigraphic record varies in step with power at those same bands in local insolation (Figs. 3d and 3f), whereas both are unique compared to power at precession and obliquity bands in the global ice volume and temperature record of Ahn (2017; Figure 3b).

## 4 Discussion

### 4.1 Heterodyne expression in the Northwest Pacific

Expression of heterodynes have been detected in other sedimentological records from the mid-latitudes of the northwest Pacific. Geological records recovered from the Chinese Loess Plateau, which are notably at similar latitudes (34°N to 42°N) to that of Hole 1207A, demonstrate variability in the monsoonal system and are also characterized by non-primary spectral peaks (e.g., Thomas et al., 2016; Cai et al., 2015; Kathayat et al., 2016; Thomas et al., 2014; Wang et al., 2008). The spectral characteristics from these Quaternary paleoclimate records display a lack of variance at the eccentricity and obliquity periods but have a concentration of variance associated with precession frequencies and the identification of significant heterodynes. Specifically, Thomas et al. (2016) argued that the existence of heterodynes demonstrates that no one single abiotic factor (e.g., summer rainfall) influenced precipitation isotope variability on the Chinese Loess Plateau during the Pleistocene. Rather, multiple regional abiotic factors (summer and winter rainfall, temperature) simultaneously influence precipitation isotope values at primary orbital periods, but in different directions and at different phases (e.g., strong winter and summer monsoons both cause precipitation isotopes to be depleted but occur at opposite precession phases). The competing interactions of multiple abiotic responses to primary insolation yield spectra with heterodynes (e.g., ~70 kyr). It is possible that the heterodynes present in Hole 1207A lithostratigraphy are also due to interactions of multiple aspects of the climate system.

The KC and the KCE make up a complex oceanic western boundary current that exerts a major control on Asian climate patterns. While observations based on satellite data demonstrate this system changes its strength and position on seasonal and interannual to decadal time scales (Yu et al., 2020), the exact mechanisms for these changes are still unknown and involve interactions between the Pacific Decadal Oscillation and El Niño-Southern Oscillation (e.g., Latif and Barnett, 1996; Zhong and Liu, 2009; Zhang et al., 1997; Newman et al., 2003; Schneider and Cornulle, 2005). On geologic time scales, changes in the strength and position of the Kuroshio Current system demonstrates clear glacial/interglacial variability (e.g., Kitamura et al., 1999; Kawahata and Ohshima, 2002; Kawahata and Ohshima, 2004; Yamamoto et al., 2005; Kitamura and Kimoto, 2006; Hoiles et al., 2012). Specifically, proxy data indicate changes in surface water hydrology, paleoproductivity, pollen accumulation, and wind intensity at sites along this frontal boundary (Kawahata and Ohshima, 2002; Venti, 2006; Venti and Billups, 2013; Venti et al., 2017; Gallagher et al., 2015; Abell et al., 2021). This variability appears to be associated with the amplification of the East Asian winter monsoon season and increased thermal gradients between low and high latitudes (Venti and Billups et al., 2013; Venti et al., 2017; Abell et al., 2021).

The position of the KCE is constrained by the southward flowing Oyashio Current to the north. This boundary is defined by the sea surface temperature gradients between the carbonate-rich subtropical and carbonate-depleted subarctic surface waters (e.g., Yu et al., 2020). Hole 1207A, currently positioned at the boundary, contains a unique sedimentary archive that reflects meridional migrations along this frontal boundary. The influence of obliquity on local insolation, and thus surface temperature, increases at higher latitudes. Whereas low-latitude insolation and

surface temperature are primarily driven by precession and modulated by eccentricity. Therefore, non-linear interactions between low- and high-latitude local insolation may influence the position that marks the transition between subtropical water and subarctic waters demonstrated by the presence of heterodynes in the lithostratigraphic record of Hole 1207A. Specifically, we suggest the heterodynes are a result of the complex interactions between eccentricity modulated low-latitude precession on the subtropical Pacific and high-latitude obliquity influence on ice volume and temperature variability, which is most pronounced prior to the MPT. Notably, this occurs during a period of maximum climate sensitivity of the tropical and subtropical regions (Ravelo et al., 2004). Our results highlight that the Hole 1207A lithostratigraphic record is most likely responding to regional circulation changes influenced by both changes in the North Equatorial Current driven by local insolation (eccentricity modulated precession) and fluctuations in the Oyashio Current driven by high-latitude climate change (obliquity) prior to the MPT (Table 4).

Cumulative spectral power plots provide a quantitative assessment of the evolution of power within orbital and heterodyne bands (Fig. 3b, d and f). Hole 1207A has the most power associated with heterodyne frequencies prior to onset of the MPT (Fig. 3f), when the ice volume record is dominated by frequencies associated with obliquity forcing (Fig. 3b). Power diminishes in the Hole 1207A heterodyne bands at ~800 ka with almost no power by 400 ka. The disappearance of heterodynes coincides with the MBE (~430 ka), when the amplitude variability of 100 kyr glacial-interglacial cycles became most extreme and the eccentricity signal dominates the ice volume record (Fig. 3b) (e.g., Jouzel et al., 2007; Yin and Berger, 2012; Yin et al., 2013; Ahn et al., 2017; Habicht, 2019). However, prior to the MPT the occurrence of heterodynes suggests that the position of the KCE is driven by the competing and of almost equal influence (Fig. 3f) over low-latitude local insolation changes modulated by eccentricity, as well as high latitude ice volume/temperature variability exerting a strong influence on the southward flowing subarctic Oyashio Current. In contrast, the lower power in the heterodynes band after the MPT suggests that low and high-latitude modulations on Northern Hemisphere insolation and ice volume/temperature, respectively, operate in phase and drive circulation changes associated with the KCE.

#### 4.2 Long-term cooling trends with superimposed periods of expansion of the subtropical gyre during late Pleistocene interglacials

The transition from dominant cluster 2 (nannofossil ooze with clay) to cluster 1 (clayey nannofossil ooze) at ~1.25 Ma (~19 mbsf) is associated with the onset of more heavy mineral deposition, reflected in the more positive values in  $\ln Zr/Sr$  and magnetic susceptibility data., Figs. 4, 5, and 8). We hypothesize this change in the lithostratigraphy represents the onset of enhanced westerlies over Hole 1207A with an increase in dust flux (heavy minerals), and/or a relative southward shift and restriction of the subtropical gyre associated with onset of the MPT (~1.25 Ma). This hypothesis is consistent with direct land-based records documenting changes in North American ice sheets suggesting a more extensive Laurentide Ice Sheet near the start of the MPT at ~1.3 Ma (Balco and Rovey, 2010), which was synchronous with colder sea surface temperatures in both the eastern equatorial upwelling regions (Liu, 2004; Liu et al., 2005; Huybers and Molnar, 2007) and in the subarctic Pacific Ocean (Martínez-García et al., 2010) (Fig. 8). This transition is also consistent with the timing of the MPT as documented from coupled Mg/Ca and  $\delta^{18}O$  benthic records inferring  $\delta^{18}O$  seawater changes in response to increases in global ice volume budgets (e.g., Elderfield et al., 2012; Ford et al., 2020).

While changes in linear sedimentation rates between age tie points represent an average rate of deposition that likely fluctuates between glacial and interglacial periods, Hole 1207A exhibits a baseline increase in linear sedimentation rates during and after the MPT (Fig. 4). This increased sedimentation rate is consistent with subarctic North Pacific Ocean records indicating an overall increase in eolian dust flux and grain size during and after the MPT due to increasing aridity across Asia and westerly wind strength over the northwest Pacific (e.g., Heslop et al., 2002; Sun and An, 2005; Yang et al., 2006; Machalett et al., 2008; Wang et al., 2016; Jia et al., 2018; Zhao et al., 2018; Lindberg et al., 2022). Similarly, such evidence for strengthening of the North Pacific westerlies has been recently documented at sites just to the north of Hole 1207A (i.e., ODP sites 885/886) across major episodes of Northern Hemisphere cooling (i.e., iNHG at 2.7 Ma; Abell et al., 2021).

Two intervals identified in the cluster lithologies and XRF normalized log-ratios indicate episodic shifts that may represent unusual warm interglacials with an expanded subtropical gyre over the last 1.25 Ma, superimposed on a long-term cooling trend (Fig. 5). Notably, these intervals stratigraphically relate to the MPT (interval 1 ~16.5–15 mbsf; 1.04–0.93 Ma) and the MBE (interval 2 ~9–5 mbsf; 0.59–0.29 Ma). They are both characterized by clear glacial-interglacial variability of cluster lithologies with stratigraphically thicker cluster 2 lithologies (nannofossil ooze with clay) representing interglacials, punctuated by decimeter- to meter-scale beds of cluster 1 lithologies (clayey nannofossil ooze) representing glacials. Thus, cluster lithologies and XRF data indicate changes in the composition of sediment supply in a pelagic setting reflecting periods of enhanced carbonate productivity with a relatively diminished supply of terrigenous wind-blown material during interglacials (Cluster 2). Whereas, glacial intervals are characterized by a relative decrease in carbonate productivity and a higher terrigenous sediment supply to Site 1207A (Cluster 1; Table 2).

In the first interval (MPT) XRF data generally indicate an increase in the amplitude of variability in wind strength proxies accompanied by a decrease in variability of surface ocean carbonate productivity from MIS 29–25 (Fig. 5). Thicker packages of the cluster 2 lithology occur within and extend to the top of the Jaramillo normal-polarity, thus corresponding with MIS 29–28. The reversed-polarity interval stratigraphically above the Jaramillo contains two more decimeter to meter-scale beds of the carbonate-rich cluster 2 lithology and corresponds to MIS 27–25. Recently, warm-season temperature variations across the MPT have been reconstructed for the Lake El'gygytyn record recovered from far east Russia and imply MIS 29, 27 and 21 were possibly warmer than MIS 31 (Lindberg et al., 2022). Thus, the timing of these warmer land-derived interglacial temperatures in the northern high-latitudes, coincides stratigraphically with the timing of subtropical gyre expansion as hypothesized from the new Hole 1207A inorganic geochemical record.

The second interval of warmth, coincides with MIS 15, and 11–9 within the Brunhes Chron, based on our untuned age model. Throughout this interval, low  $\ln$  Zr/Sr, MS and terrigenous element (Zr, Ti, and Si) counts suggests an overall relative decrease in westerly wind strength over Hole 1207A, whereas, the  $\ln$  Ca/Ti proxy indicates a period of enhanced burial of calcium carbonate (Fig. 5, 6). Similarly, high-resolution dust proxies across the north Pacific during the mid-Pliocene (i.e., ODP 885/886 and 1208), when global mean temperatures were 2-



3°C warmer than pre-industrial values, imply a decrease in dust flux and wind strength (Abell et al., 2021) and potential northward shift of the KCE and expansion of the North Pacific Subtropical Gyre (Lam et al., 2021). Results from the XRF analyses at Hole 1207A suggest that similar processes during Pleistocene interglacials, when global mean temperatures were only 1 to 2°C warmer (i.e., MIS 15, 11–9; Lang and Wolff, 2011). Thus, we hypothesize this second interval (MBE) corresponding to MIS 15 and 11–9 represents another time within the last 1.25 Ma that contains episodes of extended warmth, when the KCE shifted north of its present-day position with decreased wind strength over the midlatitudes of the North Pacific even though global mean temperatures are thought to not have exceeded 2°C.

Warmer conditions and North Pacific Subtropical Gyre expansion during MIS 11 and 9 are also recorded elsewhere in the North Pacific region (Jaccard et al., 2005). At ODP Site 882, located to the north of Hole 1207A, CaCO<sub>3</sub> content increased by more than 20% during MIS 11 and 9, in what is typically carbonate-free subarctic sediment. As Site 882 was drilled from 3243.8 meters water depth, similar to Hole 1207A (3100 meters), we infer the increased presence of carbonate is the result of warmer waters passing over Site 882. This finding suggests that expansion of the gyre may have extended as far north as 50.57°N (Jaccard et al., 2005). Notably, sea surface temperature records from the Western Pacific Warm Pool recovered from ODP Hole 806B, indicate the warmest sea surface temperatures of the last 1.4 Ma occurred during MIS 11 (Medina-Elizalde et al., 2021). This warming in the equatorial Pacific is accompanied by higher than modern precipitation patterns across the Siberian Arctic (Melles et al., 2012).

This period of subtropical gyre expansion during MIS 15 and 11–9 and excess precipitation over parts of the Northeastern Siberia may demonstrate the tight coupling between expansion of the subtropical high and displacement of the low-pressure system (Aleutian Low) delivering precipitation to the terrestrial biosphere in the high northern latitudes rather than over the Pacific Ocean. We propose that expansion of the subtropical gyre may have contributed to the unusual and enhanced warmth experienced in high latitude regions that has been documented for at least MIS 29, 27, 21, 11 and 9 (e.g., Melles et al., 2012; De Wet et al., 2016; Lindberg et al., 2022). Our data further highlights not only the role that the KCE plays in heat transport to the North Pacific (e.g., Sakamoto et al., 2005; Zhang et al., 2017; Nishikawa et al., 2020), but also the role of the subtropical high system in regulating moisture across North High Latitudes in the Pacific sector. With Pacific Ocean storm tracks positioned farther northward, moisture delivery across western North American may have been relatively greater in regions of higher elevation and latitude. Such moisture delivery could have promoted ice growth of mountain glaciers even during warm periods of the Pleistocene. Recently, similar mechanisms have been proposed through modeling experiments for growth of the Antarctic Ice Sheet during the much warmer Miocene (Halberstadt et al., 2021). Thus, the fact that these periods of warming predate times of ice volume growth is intriguing and should be further investigated using Earth System models in order to assess the feedbacks associated with changes in the configuration of the North Pacific Subtropical Gyre and North American ice volume growth across the MPT and MBE.

Lastly, episodes of an expanded North Pacific Subtropical Gyre during MISs 29 25, 15, and 11-9 do not occur under similar radiative forcing scenarios (Fig. 8). For example, a relatively expanded subtropical gyre system associated with MISs 29-25 occurs during times of high amplitude changes in orbital precession, relatively low amplitude changes in obliquity, and when

the contrast between winter (DJF) and summer (JJA) insolation is extreme at 65°N (Figure 8). Thus, alluding to a combination of processes involving enhanced tropical warming and extremes in high latitude seasonality. Whereas, interglacials of MISs 15, and 11-9 coincide with relatively small amplitude changes in orbital precession, relatively high amplitude changes in obliquity, and with low-to-moderate seasonal changes in insolation at 65°N. Such an orbital configuration would most likely have contributed to high-latitude warming with moderate seasonality changes and relatively reduced tropical warming. Such differences in radiative forcing scenarios that appear to reflect prominent changes in the subtropical gyre system may allude to the complex long-term (>100,000 years) non-linearities associated with surface ocean and atmospheric responses to some of the last periods of climate reorganization associated with the MPT and MBE.

## 5 Conclusions

Ocean Drilling Project Hole 1207A is ideally located to assess circulation changes in the northwest Pacific given that it is currently located within the transitional zone between subarctic waters to the north and subtropical waters to the south. The use of unsupervised hierarchical clustering on normalized X-ray fluorescence count data provides a useful statistical technique to demonstrate significant lithological changes at Hole 1207A that reflect long-term and orbital scale variability of paleoenvironmental conditions that are associated with the northwest Pacific Ocean western boundary current, the KCE.

Prior to the MPT the position of the KCE was significantly influenced by interactions between low latitude local insolation changes associated with precession and modulated by eccentricity, and high-latitude ice volume changes paced by obliquity. These non-linearities are identified through the existence of significant heterodyne frequencies associated with eccentricity and obliquity embedded into  $\ln$  Ca/Ti proxy data reflecting carbonate deposition as a function of the expansion and contraction of the subtropical gyre system (Fig. 4). Heterodynes in the Hole 1207A sedimentary record highlight the competing influence that modulations in low-latitude insolation and high-latitude ice-volume growth on the subtropical gyre system.

Changes in the position of the KCE over the last 2 million years has been significantly influenced by orbital forcing mechanisms with discrete intervals spanning MISs 29–25 and 15, 11–9, which demonstrate potential sustained warmth and expansion of the North Pacific Subtropical Gyre. Some of these unusual warm and persistent interglacials coincide with documented intervals of exceptional warmth in the Pacific Arctic region (Jaccard et al., 2009; Melles et al., 2012; Brigham-Grette et al., 2012; de Wet et al., 2016; Lindberg et al., 2022). Notably, these two intervals are identified by higher magnitude of glacial-interglacial variability in Cluster lithologies (higher cluster 2 to cluster 1) and XRF elemental ratios ( $\ln$  Zr/Sr and  $\ln$  Ca/Ti). These sections are interpreted as periods of pronounced warmth and an expanded subtropical gyre and coincide with time periods prior to, or surrounding episodes of increased global cooling associated with the MPT and when the amplitude of glacial cycles increased around the MBE. The different orbital forcing scenarios surrounding periods of warmth of the last 1.25 Ma allude to the complex non-linearities associated with surface ocean and atmospheric processes in the Earth System over long-time scales (>100,000 years).



## Acknowledgments

This research used samples and data provided by the Ocean Drilling Program (ODP) (currently the International Ocean Discovery Program, IODP). The IODP is sponsored by the US National Science Foundation (NSF) and participating countries under the management of Joint Oceanographic Institutions. Financial support for this project was provided by Binghamton University to M.O.P. M.O.P. and S.P.T. designed the project. All authors were critical in the interpretation of results. E.K.T. is supported by NSF grant 1652274. The authors would like to thank Nick Venti, Jordan Abell and Denise Kulhanek for useful conversations that helped with data interpretations. The authors would also like to thank Brian Levay and Mackenzie Schoemann for aiding with XRF core scanning. The authors would like to thank the shipboard science team members and crew of Ocean Drilling Program Leg 198 as the datasets they collected were central to this study. The authors would like to thank two anonymous reviewers insightful and helpful reviews that greatly improved the quality of this work.

## Open Research

All XRF elemental count data (table S1) and clustering/time series analysis code are archived on FigShare (Taylor, 2021).

## References

- Abell, J. T., Winckler, G., Anderson, R. F., & Herbert, T. D. (2021). Poleward and weakened westerlies during Pliocene warmth. *Nature* 589, 70–75.
- Ahagon, N., Tanaka, Y., & Ujiie, H. (1993). *Florisphaera profunda*, a possible nannoplankton indicator of late Quaternary changes in sea-water turbidity at the northwestern margin of the Pacific. *Marine Micropaleontology*, 22(3), 255–273.
- Ahn, S., Khider, D., Lisiecki, L. E., & Lawrence, C. E. (2017). A probabilistic Pliocene–Pleistocene stack of benthic  $\delta^{18}\text{O}$  using a profile hidden Markov model. *Dynamics and Statistics of the Climate System*, 2(1).
- Andres, M., Jan, S., Sanford, T. B., Mensah, V., Centurioni, L. R., & Book, J. W. (2015). Mean structure and variability of the Kuroshio from northeastern Taiwan to southwestern Japan. *Oceanography*, 28(4), 84-95.
- Arz, H. W., Pätzold, J., & Wefer, G. (1998). Correlated Millennial-Scale Changes in Surface Hydrography and Terrigenous Sediment Yield Inferred from Last-Glacial Marine Deposits off Northeastern Brazil. *Quaternary Research*, 50(2), 157–166.
- Arz, H. W., Pätzold, J., & Wefer, G. (1999). Climatic changes during the last deglaciation recorded in sediment cores from the northeastern Brazilian Continental Margin. *Geo-Marine Letters*, 19(3), 209-218.
- Augustin, L., Barbante, C., Barnes, P. R., Barnola, J. M., Bigler, M., Castellano, E., ... & Zucchelli, M. (2004). Eight glacial cycles from an Antarctic ice core. *Nature*, 429, 623-628.

Bahr, A., Lamy, F., Arz, H., Kuhlmann, H., & Wefer, G. (2005). Late glacial to Holocene climate and sedimentation history in the NW Black Sea. *Marine Geology*, 214(4), 309-322.

Bahr, A., Lamy, F., Arz, H. W., Major, C., Kwiecien, O., & Wefer, G. (2008). Abrupt changes of temperature and water chemistry in the late Pleistocene and early Holocene Black Sea. *Geochemistry, Geophysics, Geosystems*, 9(1).

Bahr, A., Jiménez-Espejo, F. J., Kolasinac, N., Grunert, P., Hernández-Molina, F. J., Röhl, U., Voelker, A. H. L., Escutia, C., Stow, D. A. V., Hodell, D., & Alvarez-Zarikian, C. A. (2014). Deciphering bottom current velocity and paleoclimate signals from contourite deposits in the Gulf of Cádiz during the last 140 kyr: An inorganic geochemical approach. *Geochemistry, Geophysics, Geosystems*, 15(8), 3145–3160.

Balco, G., & Rovey, C. W. (2010). Absolute chronology for major Pleistocene advances of the Laurentide Ice Sheet. *Geology*, 38(9), 795–798. <https://doi.org/10.1130/G30946.1>.

Becquey, S., & Gersonde, R. (2002). Past hydrographic and climatic changes in the Subantarctic Zone of the South Atlantic—The Pleistocene record from ODP Site 1090. *Palaeogeography, Palaeoclimatology, Palaeoecology*, 182(3-4), 221-239.

Berg, S., Wagner, B., White, D. A., & Melles, M. (2010). No significant ice-sheet expansion beyond present ice margins during the past 4500 yr at Rauer Group, East Antarctica. *Quaternary Research*, 74(1), 23–25. Cambridge Core.

Berger, W. H., & Wefer, G. (2003). On the dynamics of the ice ages: Stage-11 paradox, mid-Brunhes climate shift, and 100-ky cycle. *GEOPHYSICAL MONOGRAPH-AMERICAN GEOPHYSICAL UNION*, 137, 41-60.

Bialik, O. M., Jarochowska, E., & Grossowicz, M. (2021). Ordination analysis in sedimentology, geochemistry and palaeoenvironment—Background, current trends and recommendations. *The Depositional Record*, 7(3), 541-563.

Bindoff, N. L., Cheung, W. W. L., Kairo, J. G., Arístegui, J., Guinder, Valeria A., Hallberg, R., Hilmi, N. J. M., Jiao, N., Karim, M. S. Levin, L., O'Donoghue, S., Purca C., Sara R., Rinkevich, B., Suga, T., Tagliabue, A., & Williamson, P. (Eds.) *IPCC Special Report on the Ocean and Cryosphere in a Changing Climate*. Intergovernmental Panel on Climate Change, Switzerland, pp. 477-587.

Blain, H. A., Cuenca-Bescós, G., Lozano-Fernández, I., López-García, J. M., Ollé, A., Rosell, J., & Rodríguez, J. (2012). Investigating the Mid-Brunhes Event in the Spanish terrestrial sequence. *Geology*, 40(11), 1051-1054.

Bourget, J., Zaragosi, S., Garlan, T., Gabelotaud, I., Guyomard, P., Dennielou, B., Ellouz-Zimmerman, N., & Schneider, J. L. (2008). Discovery of a giant deep-sea valley in the Indian Ocean, off eastern Africa: the Tanzania channel. *Marine Geology*, 255(3-4), 179-185.

Bralower, T. J., Premoli Silva, I., & Malone, M. J. (Eds.). (2006). *Proceedings of the Ocean Drilling Program, 198 Scientific Results* (Vol. 198). Ocean Drilling Program.

Brigham-Grette, J., Melles, M., Minyuk, P., Andreev, A., Tarasov, P., DeConto, R., Koenig, S., Nowaczyk, N., Wennrich, V., Rosén, P., Haltia, E., Cook, T., Gebahardt, C., Meyer-Jacob, C., Snyder, J. & Herzschuh, U. (2013). Pliocene Warmth, Polar Amplification, and Stepped Pleistocene Cooling Recorded in NE Arctic Russia. *Science*, 340(6139), 1421–1427.

Caballero-Gill, R. P., Herbert, T. D., & Dowsett, H. J. (2019). 100-kyr Paced Climate Change in the Pliocene Warm Period, Southwest Pacific. *Paleoceanography and Paleoclimatology*, 34(4), 524–545.

Cai, W., Santoso, A., Wang, G., Sang-Wook, Y., Soon-II, A., Cobb, K. M., Collins, M., Guilyardi, E., Jin, F., Kug, J., Lengaigne, M., McPhaden, M. J., Takahashi, K., Timmermann, A., Vecchi, G., Watanabe, M. & Wu, L. (2015). ENSO and greenhouse warming. *Nature Clim Change* 5, 849–859.

Chen, C., Beardsley, R. C., & Limeburner, R. (1992). The structure of the Kuroshio southwest of Kyushu: Velocity, transport and potential vorticity fields. *Deep Sea Research Part A. Oceanographic Research Papers*, 39(2), 245–268.

Chen, J., Chen, Y., Liu, L., Ji, J., Balsam, W., Sun, Y., & Lu, H. (2006). Zr/Rb ratio in the 767 Chinese loess sequences and its implication for changes in the East Asian winter monsoon 768 strength. *Geochimica et Cosmochimica Acta*, 70(6), 1471-1482.

Clemens, S., Prell, W., & Sun, Y. (2010). Orbital-scale timing and mechanisms driving Late Pleistocene Indo-Asian summer monsoons: Reinterpreting cave speleothem ?? 18 O. *Paleoceanography*, 25.

Croudace, I. W., & Rothwell, R. G. (Eds.). (2015). *Micro-XRF Studies of Sediment Cores: Applications of a non-destructive tool for the environmental sciences* (Vol. 17). Springer. da Silva, A. M., Young, C. C., & Levitus, S. (1994). Atlas of surface marine data 1994, Vol. 1: Algorithms and procedures. *Noaa atlas nesdis*, 6(83), 20910-3282.

De Wet, G., Castañeda, I., DeConto, R., & Brigham-Grette, J. (2016). A high-resolution mid Pleistocene temperature record from Arctic Lake El'gygytgyn: A 50 kyr super interglacial from MIS 33 to MIS 31? *Earth and Planetary Science Letters*, 436, 56–63.

Deser, C., Alexander, M. A., & Timlin, M. S. (1999). Evidence for a wind-driven intensification of the Kuroshio Current Extension from the 1970s to the 1980s. *Journal of Climate*, 12(6), 1697-1706.

Dunlea, A. G., Murray, R. W., Tada, R., Alvarez- Zarikian, C. A., Anderson, C. H., Gilli, A., ... & Ziegler, M. (2020). Intercomparison of XRF core scanning results from seven labs and approaches to practical calibration. *Geochemistry, Geophysics, Geosystems*, 21(9).

Dutkiewicz, A., Müller, R. D., O'Callaghan, S., & Jónasson, H. (2015). Census of seafloored sediments in the world's ocean. *Geology*, 43(9), 795-798.

Elderfield, H., Ferretti, P., Greaves, M., Crowhurst, S., McCave, I. N., Hodell, D., & Piotrowski, A. M. (2012). Evolution of ocean temperature and ice volume through the mid-Pleistocene climate transition. *science*, 337(6095), 704-709.

Evans, H. F., Channell, J. E., & Sager, W. W. (2005). Late Miocene–Holocene magnetic polarity stratigraphy and astrochronology, ODP Leg 198, Shatsky Rise. In *Proceedings of the ocean drilling program, scientific results* (Vol. 198, pp. 1-39).

Fedorov, A. V., Brierley, C. M., Lawrence, K. T., Liu, Z., Dekens, P. S., & Ravelo, A. C. (2013). Patterns and mechanisms of early Pliocene warmth. *Nature*, 496(7443), 43-49.

Ford, H. L., Sosdian, S. M., Rosenthal, Y., & Raymo, M. E. (2016). Gradual and abrupt changes during the Mid-Pleistocene Transition. *Quaternary Science Reviews*, 148, 222-233. Ford, H. L., & Chalk, T. B. (2020). The Mid-Pleistocene Enigma. *Oceanography*, 33(2), 101-103.

Ford, H. L., & Raymo, M. E. (2020). Regional and global signals in seawater  $\delta^{18}\text{O}$  records across the mid-Pleistocene transition. *Geology*, 48(2), 113-117.

Frankignoul, C., & Sennéchaël, N. (2007). Observed influence of North Pacific SST anomalies on the atmospheric circulation. *Journal of Climate*, 20(3), 592-606.

Gallagher, S. J., Kitamura, A., Iryu, Y., Itaki, T., Koizumi, I., & Hoiles, P. W. (2015). The Pliocene to recent history of the Kuroshio and Tsushima Currents: a multi-proxy approach. *Progress in Earth and Planetary Science*, 2(1), 1-23.

Gruetzner, J., & Higgins, S. M. (2010). Threshold behavior of millennial scale variability in deep water hydrography inferred from a 1.1 Ma long record of sediment provenance at the southern Gardar Drift. *Paleoceanography*, 25(4)

Habicht, M. H. (2019). *Middle to Late Pleistocene Paleoenvironmental Reconstructions from Lake El'gygytgyn, Arctic Russia* (Doctoral dissertation, University of Massachusetts Libraries).

Halberstadt, A.R.W., Chorley, H., Levy, R.H., Naish, T., DeConto, R.M., Gasson, E. and Kowalewski, D.E., 2021. CO<sub>2</sub> and tectonic controls on Antarctic climate and ice-sheet evolution in the mid-Miocene. *Earth and Planetary Science Letters*, 564, p.116908.

Hammer, Ø., Harper, D.A.T., and Ryan, P. D. (2001). PAST: Paleontological Statistics Software Package for Education and Data Analysis. *Palaeontologia Electronica*, 4(1): 9pp.

Haug, G. H., Ganopolski, A., Sigman, D. M., Rosell-Mele, A., Swann, G. E. A., Tiedermann, R., Jaccard, S. L., Bollmann, J., Maslin, M. A., Leng, M. J. & Eglinton G. (2005). North Pacific seasonality and the glaciation of North America 2.7 million years ago. *Nature*, 433(7028), 821-825.

- Heslop, D., Dekkers, M. J., & Langereis, C. G. (2002). Timing and structure of the mid Pleistocene transition: records from the loess deposits of northern China. *Palaeogeography, Palaeoclimatology, Palaeoecology*, 185(1-2), 133-143.
- Hodell, D. A., Evans, H. F., Channell, J. E., & Curtis, J. H. (2010). Phase relationships of North Atlantic ice-rafted debris and surface-deep climate proxies during the last glacial period. *Quaternary Science Reviews*, 29(27-28), 3875-3886.
- Hoiles, P. W., Gallagher, S. J., Kitamura, A., & Southwood, J. M. (2012). The evolution of the Tsushima Current during the early Pleistocene in the Sea of Japan: An example from marine isotope stage (MIS) 47. *Global and Planetary Change*, 92, 162-178.
- Hu, D., Wu, L., Cai, W., Gupta, A. S., Ganachaud, A., Qiu, B., Gordon, A. L., Lin, X., Chen, Z., Hu, S., Wang, G., Wang, Q., Sprintall, J., Tangdong, Q., Kashino, Y., Wang, F. & Kessler, W. S. (2015). Pacific western boundary currents and their roles in climate. *Nature*, 522(7556), 299-308.
- Hudson, A. M., Hatchett, B. J., Quade, J., Boyle, D. P., Bassett, S. D., Ali, G., & Marie, G. (2019). North-south dipole in winter hydroclimate in the western United States during the last deglaciation. *Scientific reports*, 9(1), 1-12.
- Huybers, P., & Molnar, P. (2007). Tropical cooling and the onset of North American glaciation. *Climate of the Past*, 3(3), 549-557.
- Imawaki, S., Bower, A. S., Beal, L., & Qiu, B. (2013). Western boundary currents. In *International Geophysics* (Vol. 103, pp. 305-338). Academic Press.
- Ingram, W. C., Meyers, S. R., Brunner, C. A., & Martens, C. S. (2010). Late Pleistocene-Holocene sedimentation surrounding an active seafloor gas-hydrate and cold-seep field on the Northern Gulf of Mexico slope. *Marine Geology*, 278, 45-53.
- IPCC. (2021). Climate Change 2021: The Physical Science Basis. Contribution of Working Group I to the Sixth Assessment Report of the Intergovernmental Panel on Climate Change [Masson-Delmotte, V., P. Zhai, A. Pirani, S.L. Connors, C. Péan, S. Berger, N. Caud, Y. Chen, L. Goldfarb, M.I. Gomis, M. Huang, K. Leitzell, E. Lonnoy, J.B.R. Matthews, T.K. Maycock, T. Waterfield, O. Yelekçi, R. Yu, and B. Zhou (eds.)]. Cambridge University Press. In Press.
- Isono, D., Yamamoto, M., Irino, T., Oba, T., Murayama, M., Nakamura, T., & Kawahata, H. (2009). The 1500-year climate oscillation in the midlatitude North Pacific during the Holocene. *Geology*, 37(7), 591-594.
- Ito, M., & Horikawa, K. (2000). Millennial-to decadal-scale fluctuation in the paleo-Kuroshio Current documented in the Middle Pleistocene shelf succession on the Boso Peninsula, Japan. *Sedimentary Geology*, 137(1-2), 1-8.



- Jaccard, S. L., Haug, G. H., Sigman, D. M., Pedersen, T. F., Thierstein, H. R., & Röhl, U. (2005). Glacial/interglacial changes in subarctic North Pacific stratification. *Science*, *308*(5724), 1003-1006.
- Jaccard, S. L., Galbraith, E. D., Sigman, D. M., Haug, G. H., Francois, R., Pedersen, T. F., Dulski, P., & Thierstein, H. R. (2009). *Geochemistry of ODP Site 145-882*. PANGAEA.
- Jacobi, R. D., & Hayes, D. E. (1989). Sedimentary effects of interplay between the Kuroshio Extension and Pacific plate motion. *Geological Society of America Bulletin*, *101*(4), 549-560.
- Jaeschke, A., Rühlemann, C., Arz, H., Heil, G., & Lohmann, G. (2007). Coupling of millennial-scale changes in sea surface temperature and precipitation off northeastern Brazil with high-latitude climate shifts during the last glacial period. *Paleoceanography*, *22*(4).
- Jansen, J. H. F., Kuijpers, A., & Troelstra, S. R. (1986). A mid-Brunhes climatic event: long-term changes in global atmosphere and ocean circulation. *Science*, *232*(4750), 619-622.
- Jansen, J. H. F., Van der Gaast, S. J., Koster, B., & Vaars, A. J. (1998). CORTEX, a shipboard XRF-scanner for element analyses in split sediment cores. *Marine geology*, *151*(1-4), 143-153.
- Jia, J., Lu, H., Wang, Y., & Xia, D. (2018). Variations in the iron mineralogy of a loess section in Tajikistan during the Mid- Pleistocene and Late Pleistocene: Implications for the climatic evolution in central Asia. *Geochemistry, Geophysics, Geosystems*, *19*(4), 1244-1258.
- Jian, Z. (1998). Stable isotopic records of the glacial deep-water properties in the South China Sea. *Science in China Series D: Earth Sciences*, *41*(4), 337-344.
- Jian, Z., Wang, P., Saito, Y., Wang, J., Pflaumann, U., Oba, T., & Cheng, X. (2000). Holocene variability of the Kuroshio current in the Okinawa Trough, northwestern Pacific Ocean. *Earth and Planetary Science Letters*, *184*(1), 305-319.
- Jimenez-Espejo, F. J., Presti, M., Kuhn, G., McKay, R., Crosta, X., Escutia, C., Lucci, R. G., Tolotti, R., Yoshimura, T., Huertas, M. O., Marcrì, P., Caburlotto, A. & De Santis, L. (2020). Late Pleistocene oceanographic and depositional variations along the Wilkes Land margin (East Antarctica) reconstructed with geochemical proxies in deep-sea sediments. *Global and planetary change*, *184*, 103045.
- Jouzel, J., Masson-Delmotte, V., Cattani, O., Dreyfus, G., Falourd, S., Hoffman, G., Minster, B., Nouet, J., Barnola, J. M., Chappellaz, J., Fischer, H., Gallet, J. C., Johnsen, S., Leuenberger, M., Loulergue, L., Luethi, D., Oerter, H., Parrenin, F., Raisbeck, G., Raynaud, D., Schilt, A., Schwander, J., Selmo, E., Souchez, R., Spani, R., Stauffer, B., Steffensen, J. P., Stenni, B., Stocker, T. F., Tison, J. L., Werner, M. & Wolff, E. W. (2007). Orbital and millennial Antarctic climate variability over the past 800,000 years. *Science*, *317*(5839), 793-796.
- Kathayat, G., Cheng, H., Sinha, A., Spötl, C., Edwards, R. L., Zhang, H., Li, X., Yi, L., Cai, Y., Lui, W. L. & Breitenbach, S. F. M. (2016). Indian monsoon variability on millennial-orbital



timescales. *Scientific reports*, 6(1), 1-7.

Kawahata, H., & Ohshima, H. (2002). Small latitudinal shift in the Kuroshio Extension (Central Pacific) during glacial times: evidence from pollen transport. *Quaternary Science Reviews*, 21(14-15), 1705-1717.

Kawahata, H., & Ohshima, H. (2004). Vegetation and environmental record in the northern East China Sea during the late Pleistocene. *Global and Planetary Change*, 41(3-4), 251-273.

Kitamura, A., & Kimoto, K. (2006). History of the inflow of the warm Tsushima Current into the Sea of Japan between 3.5 and 0.8 Ma. *Palaeogeography, Palaeoclimatology, Palaeoecology*, 236(3-4), 355-366.

Kitamura, A., Matsui, H., & Oda, M. (1999). Change in the thickness of the warm Tsushima Current at the initiation of its flow into the Sea of Japan. *Palaeogeography, Palaeoclimatology, Palaeoecology*, 152(3-4), 305-318.

Kwiecien, O., Arz, H. W., Lamy, F., Plessen, B., Bahr, A., & Haug, G. H. (2009). North Atlantic control on precipitation pattern in the eastern Mediterranean/Black Sea region during the last glacial. *Quaternary Research*, 71(3), 375-384.

Kwon, Y. O., & Joyce, T. M. (2013). Northern Hemisphere winter atmospheric transient eddy heat fluxes and the Gulf Stream and Kuroshio–Oyashio Extension variability. *Journal of Climate*, 26(24), 9839-9859.

Lam, A. R., & Leckie, R. M. (2020a). Late Neogene and Quaternary diversity and taxonomy of subtropical to temperate planktic foraminifera across the Kuroshio Current Extension, northwest Pacific Ocean. *Micropaleontology*, 66(3), 177-268.

Lam, A. R., & Leckie, R. M. (2020b). Subtropical to temperate late Neogene to Quaternary planktic foraminiferal biostratigraphy across the Kuroshio Current Extension, Shatsky Rise, northwest Pacific Ocean. *Plos one*, 15(7), e0234351.

Lam, A. R., Leckie, R. M., & Patterson, M. O. (2020). Illuminating the Past to See the Future of Western Boundary Currents. *Oceanography*, 33(2), 65-67.

Lam, A. R., MacLeod, K. G., Schilling, S. H., Leckie, R. M., Fraass, A. J., Patterson, M. O., & Venti, N. L. (2021). Pliocene to earliest Pleistocene (5–2.5 Ma) Reconstruction of the Kuroshio Current Extension Reveals a Dynamic Current. *Paleoceanography and Paleoclimatology*, e2021PA004318.

Lang, N., & Wolff, E. W. (2011). Interglacial and glacial variability from the last 800 ka in marine, ice and terrestrial archives. *Climate of the Past*, 7(2), 361-380.

Laskar, J., Robutel, P., Joutel, F., Gastineau, M., Correia, A. C. M., & Levrard, B. (2004). A long-term numerical solution for the insolation quantities of the Earth. *Astronomy & Astrophysics*, 428(1), 261-285.

Latif, M., & Barnett, T. P. (1994). Causes of decadal climate variability over the North Pacific and North America. *Science*, 266(5185), 634-637.

Latif, M., & Barnett, T. P. (1996). Decadal climate variability over the North Pacific and North America: Dynamics and predictability. *Journal of Climate*, 9(10), 2407-2423.

Lindberg, K. R., Daniels, W. C., Castañeda, I. S., & Brigham-Grette, J. (2022). Biomarker proxy records of Arctic climate change during the Mid-Pleistocene transition from Lake El'gygytgyn (Far East Russia). *Climate of the Past*, 18(3), 559-577.

Liang, L., Sun, Y., Beets, C. J., Prins, M. A., Wu, F., & Vandenberghe, J. (2013). Impacts of grain size sorting and chemical weathering on the geochemistry of Jingyuan loess in the northwestern Chinese Loess Plateau. *Journal of Asian Earth Sciences*, 69, 177-184.

Lisiecki, L. E., & Raymo, M. E. (2005). A Pliocene-Pleistocene stack of 57 globally distributed benthic  $\delta^{18}\text{O}$  records. *Paleoceanography*, 20(1).

Liu, Z. (2004). *Pleistocene climate evolution in the eastern Pacific and implications for the orbital theory of climate change*. Brown University.

Liu, L., Chen, J., Chen, Y., Ji, J., & Lu, H. (2002). Variation of Zr/Rb ratios on the Loess Plateau of Central China during the last 130000 years and its implications for winter monsoon. *Chinese Science Bulletin*, 47(15), 1298-1302.

Liu, Z., Altabet, M. A., & Herbert, T. D. (2005). Glacial-interglacial modulation of eastern tropical North Pacific denitrification over the last 1.8-Myr. *Geophysical Research Letters*, 32(23).

Locarini, R. A., Mishonov, A. V., & Antonov, J. I. (2013). World Ocean Atlas 2013, Volume 1: Temperature (NOAA Atlas NESDIS 73). *Silver Spring, MD: NOAA*, 40.

Long, Y., Zhu, X. H., & Guo, X. (2019). The Oyashio nutrient stream and its nutrient transport to the mixed water region. *Geophysical Research Letters*, 46(3), 1513-1520.

Lyle, M., Barron, J., Bralower, T. J., Huber, M., Olivarez Lyle, A., Ravelo, A. C., ... & Wilson, P. A. (2008). Pacific Ocean and Cenozoic evolution of climate. *Reviews of Geophysics*, 46(2).

Machalett, B., Oches, E. A., Frechen, M., Zöller, L., Hambach, U., Mavlyanova, N. G., ... & Endlicher, W. (2008). Aeolian dust dynamics in central Asia during the Pleistocene: Driven by the long-term migration, seasonality, and permanency of the Asiatic polar front. *Geochemistry, Geophysics, Geosystems*, 9(8).

Mann, M. E., & Lees, J. M. (1996). Robust estimation of background noise and signal detection in climatic time series. *Climatic change*, 33(3), 409-445.

Martínez-García, A., Rosell-Melé, A., McClymont, E. L., Gersonde, R., & Haug, G. H. (2010). Subpolar link to the emergence of the modern equatorial Pacific cold tongue. *Science*,

328(5985), 1550-1553.

McCarron, A. P., Bigg, G. R., Brooks, H., Leng, M. J., Marshall, J. D., Ponomareva, V., Portnyagin, M., Reimer, P. J., and Rogerson, M. (2021). Northwest Pacific ice-rafted debris at 38°N reveals episodic ice-sheet change in late Quaternary Northeast Siberia. *Earth and Planetary Science Letters*, 553, <https://doi.org/10.1016/j.epsl.2020.116650>

McGee, D., Moreno-Chamarro, E., Marshall, J., & Galbraith, E. D. (2018). Western US lake expansions during Heinrich stadials linked to Pacific Hadley circulation. *Science advances*, 4(11), eaav0118.

Medina-Elizalde, M., Perritano, S., DeCesare, M., Polanco-Martinez, J., Serrato-Marks, G., McGee, D., & Lasas-Hernandez, F. (2021). Holocene Hydroclimate in the Southeastern United States During Abrupt Climate Events: Evidence From New Speleothem Isotopic Records From Alabama.

Melles, M., Brigham-Grette, J., Minyuk, P. S., P. S., Nowaczyk, N. R., Wennrich, V., DeConto, R. M., Anderson, P. M., Andreev, A. A., Coletti, A., Cook, T. L., Haltia-Hovi, E., Kukkonen, M., Lozhkin, A. V., Rosén, P., Tarasov, P., Vogel, H. & Wagner, B. (2012). 2.8 million years of Arctic climate change from Lake El'gygytyn, NE Russia. *science*, 337(6092), 315-320.

Meyers, S. R., Sageman, B. B., & Hinnov, L. A. (2001). Integrated quantitative stratigraphy of the Cenomanian-Turonian Bridge Creek Limestone Member using evolutive harmonic analysis and stratigraphic modeling. *Journal of Sedimentary Research*, 71(4), 628-644.

Meyers, S. R. (2012). Seeing red in cyclic stratigraphy: Spectral noise estimation for astrochronology. *Paleoceanography*, 27(3).

Meyers S. R. (2014). *Astrochron: An R Package for Astrochronology*.

Meyers, S. R. (2015). The evaluation of eccentricity- related amplitude modulation and bundling in paleoclimate data: An inverse approach for astrochronologic testing and time scale optimization. *Paleoceanography*, 30(12), 1625-1640.

Meyers, S. R. (2019). Cyclostratigraphy and the problem of astrochronologic testing. *Earth-Science Reviews*, 190, 190-223.

Miller, A. J., Cayan, D. R., & White, W. B. (1998). A westward-intensified decadal change in the North Pacific thermocline and gyre-scale circulation. *Journal of Climate*, 11(12), 3112-3127.

Nakamura, H., Sampe, T., Tanimoto, Y., & Shimpo, A. (2004). Observed associations among storm tracks, jet streams and midlatitude oceanic fronts. *Earth's Climate: The Ocean-Atmosphere Interaction, Geophys. Monogr*, 147, 329-345.

Newman, M., Compo, G. P., & Alexander, M. A. (2003). ENSO-forced variability of the Pacific decadal oscillation. *Journal of Climate*, 16(23), 3853-3857.

Nishikawa, H., Nishikawa, S., Ishizaki, H., Wakamatsu, T., & Ishikawa, Y. (2020). Detection of the Oyashio and Kuroshio fronts under the projected climate change in the 21<sup>st</sup> century. *Progress in Earth and Planetary Science*, 7(1), 1-12.

Owen, R.B., Muiruri, V.M., Lowenstein, T.K., Renaut, R.W., Rabideaux, N., Luo, S., Deino, A.L., Sier, M.J., Dupont-Nivet, G., McNulty, E.P. and Leet, K., 2018. Progressive aridification in East Africa over the last half million years and implications for human evolution. *Proceedings of the National Academy of Sciences*, 115(44), pp.11174-11179.

Patterson, M. O., McKay, R., Naish, T., Escutia, C., Jimenez-Espejo, F. J., Raymo, M. E., Meyers, S. R., Tauxe, L., Brinkhuis, H., IODP Expedition 318 Scientists (2014). Orbital forcing of the East Antarctic ice sheet during the Pliocene and Early Pleistocene. *Nature Geoscience*, 7(11), 841-847.

Penkrot, M. L., Jaeger, J. M., Cowan, E. A., St-Onge, G., & LeVay, L. (2018). Multivariate modeling of glacial marine lithostratigraphy combining scanning XRF, multisensory core properties, and CT imagery: IODP Site U1419. *Geosphere*, 14(4), 1935-1960.

Piva, A., Asioli, A., Schneider, R. R., Trincardi, F., Andersen, N., Colmenero-Hidalgo, E., Dennielou, B., Flores, J.-A., & Vigliotti, L. (2008). Climatic cycles as expressed in sediments of the PROMESSI borehole PRAD1-2, central Adriatic, for the last 370 ka: 1. Integrated Stratigraphy. *Geochemistry Geophysics Geosystems*, 9(1), doi:10.1029/2007GC001713

Proistosescu, C., Huybers, P., & Maloof, A. C. (2012). To tune or not to tune: Detecting orbital variability in Oligo-Miocene climate records. *Earth and Planetary Science Letters*, 325, 100-107.

R Core Team (2017) R: A Language and Environment for Statistical Computing.

Ravelo, A. C., Andreasen, D. H., Lyle, M., Lyle, A. O., & Wara, M. W. (2004). Regional climate shifts caused by gradual global cooling in the Pliocene epoch. *Nature*, 429(6989), 263-267.

Raymo, M. E., & Nisancioglu, K. H. (2003). The 41 kyr world: Milankovitch's other unsolved mystery. *Paleoceanography*, 18(1).

Reilly, B. T., Tauxe, L., Brachfeld, S., Raymo, M., Bailey, I., Hemming, S., (2021). New magnetostratigraphic insights from Iceberg Alley on the rhythms of Antarctic climate during the Plio-Pleistocene. *Paleoceanography and Paleoclimatology*, 36(2), e2020PA003994.

Rial, J. A., & Anaclerio, C. A. (2000). Understanding nonlinear responses of the climate system to orbital forcing. *Quaternary Science Reviews*, 19(17-18), 1709-1722.

Sager, W. W., Zhang, J., Korenaga, J., Sano, T., Koppers, A. A., Widdowson, M., & Mahoney, J. J. (2013). An immense shield volcano within the Shatsky Rise oceanic plateau, northwest Pacific Ocean. *Nature Geoscience*, 6(11), 976-981.

- Sakamoto, T. T., Hasumi, H., Ishii, M., Emori, S., Suzuki, T., Nishimura, T., & Sumi, A. (2005). Responses of the Kuroshio and the Kuroshio Extension to global warming in a high-resolution climate model. *Geophysical Research Letters*, 32(14).
- Sakurai, Y. (2007). An overview of the Oyashio ecosystem. *Deep Sea Research Part II: Topical Studies in Oceanography*, 54(23-26), 2526-2542.
- Schlitzer, R., Anderson, R. F., Dodas, E. M., Lohan, M., Geibert, W., Tagliabue, A., ... & Lechtenfeld, O. J. (2018). The GEOTRACES intermediate data product 2017. *Chemical Geology*, 493, 210-223.
- Schneider, N., & Cornuelle, B. D. (2005). The forcing of the Pacific decadal oscillation. *Journal of Climate*, 18(21), 4355-4373.
- Shackleton, N. J., & Opdyke, N. D. (1977). Oxygen isotope and palaeomagnetic evidence for early Northern Hemisphere glaciation. *Nature*, 270(5634), 216-219.
- St. John, K. E. K., & Krissek, L. A. (1999). Regional patterns of Pleistocene ice-rafted debris flux in the North Pacific. *Paleoceanography*, 14(5), 653–662.
- Sun, Y., & An, Z. (2005). Late Pliocene- Pleistocene changes in mass accumulation rates of eolian deposits on the central Chinese Loess Plateau. *Journal of Geophysical Research: Atmospheres*, 110(D23).
- Sutherland, R. (2019). Expedition 371 summary.
- Taylor, Shawn (2021): Hole 1207A (0-2.2 Ma) XRF Paleoceanography and Paleoclimatology Files. Figshare. [Collection]. <https://doi.org/10.6084/m9.figshare.c.5719136.v1>
- Templ, M., Filzmoser, P., & Reimann, C. (2008). Cluster analysis applied to regional geochemical data: problems and possibilities. *Applied Geochemistry*, 23(8), 2198-2213.
- Thomas, E.K., Clemens, S.C., Prell, W.L., Herbert, T.D., Huang, Y., Liu, Z., Damsté, J.S.S., Sun, Y. & Wen X. Temperature and leaf wax  $\delta^2\text{H}$  records demonstrate seasonal and regional controls on Asian monsoon proxies *Geology*, 42 (2014), pp. 1075-1078.
- Thomas, E. K., Clemens, S. C., Sun, Y., Prell, W. L., Huang, Y., Gao, L., Loomis, S., Chen, G. & Liu, Z. (2016). Heterodynes dominate precipitation isotopes in the East Asian monsoon region, reflecting interaction of multiple climate factors. *Earth and Planetary Science Letters*, 455, 196-206.
- Tjallingii, R., Röhl, U., Kölling, M., & Bickert, T. (2007). Influence of the water content on X-ray fluorescence core-scanning measurements in soft marine sediments. *Geochemistry, Geophysics, Geosystems*, 8(2).
- Tjallingii, R., Stattegger, K., Wetzel, A., & Van Phach, P. (2010). Infilling and flooding of the



- Mekong River incised valley during deglacial sea-level rise. *Quaternary Science Reviews*, 29(11-12), 1432-1444.
- Tzedakis, P. C., Raynaud, D., McManus, J. F., Berger, A., Brovkin, V., & Kiefer, T. (2009). Interglacial diversity. *Nature Geoscience*, 2(11), 751-755.
- Ujiié, H. (2003). A 370-ka paleoceanographic record from the Hess Rise, central North Pacific Ocean, and an indistinct 'Kuroshio Extension.' *Marine Micropaleontology*, 49, 21-47.
- Ujiié, H., & Ujiié, Y. (1999). Late Quaternary course changes of the Kuroshio Current in the Ryukyu Arc region, northwestern Pacific Ocean. *Marine Micropaleontology*, 37(1), 23-40.
- Van Hoang, L., Clift, P. D., Schwab, A. M., Huuse, M., Nguyen, D. A., & Zhen, S. (2010). Large-scale erosional response of SE Asia to monsoon evolution reconstructed from sedimentary records of the Song Hong-Yinggehai and Qiongdongnan basins, South China Sea. *Geological Society, London, Special Publications*, 342(1), 219-244.
- Venti, N. L., & Billups, K. (2013). Surface water hydrography of the Kuroshio Extension during the Pliocene–Pleistocene climate transition. *Marine Micropaleontology*, 101, 106-114.
- Venti, N. L., Billups, K., & Herbert, T. D. (2013). Increased sensitivity of the Plio-Pleistocene northwest Pacific to obliquity forcing. *Earth and Planetary Science Letters*, 384, 121-131.
- Venti, N. L., Billups, K., & Herbert, T. D. (2017). Paleoproductivity in the northwestern Pacific Ocean during the Pliocene-Pleistocene climate transition (3.0–1.8 Ma). *Paleoceanography*, 32(2), 92-103.
- Venti, N. L., Leckie, R. M., & Evans, H. F. (2006, December). Revised late Neogene mid-latitude planktic foraminiferal biostratigraphy for the northwest Pacific (Shatsky Rise), ODP leg 198. In *AGU Fall Meeting Abstracts* (Vol. 2006, pp. PP23B-1750).
- Wang, B., & Zhou, X. (2008). Climate variation and prediction of rapid intensification in tropical cyclones in the western North Pacific. *Meteorology and Atmospheric Physics*, 99(1), 1-16.
- Wang, P., Tian, J., Cheng, X., Liu, C., & Xu, J. (2003). Carbon reservoir changes preceded major ice-sheet expansion at the mid-Brunhes event. *Geology*, 31(3), 239-242.
- Wang, X., Wei, H., Taheri, M., Khormali, F., Danukalova, G., & Chen, F. (2016). Early Pleistocene climate in western arid central Asia inferred from loess-palaeosol sequences. *Scientific Reports*, 6(1), 1-9.
- Weedon, G. P. (2003). *Time-series analysis and cyclostratigraphy: examining stratigraphic records of environmental cycles*. Cambridge University Press.
- Weltje, G. J., & Tjallingii, R. (2008). Calibration of XRF core scanners for quantitative geochemical logging of sediment cores: Theory and application. *Earth and Planetary Science Letters*, 274(3-4), 423-438.



- Westerhold, T., Röhl, U., McCarren, H. K., & Zachos, J. C. (2009). Latest on the absolute age of the Paleocene-Eocene Thermal Maximum (PETM): new insights from exact stratigraphic position of key ash layers +19 and -17. *Earth and Planetary Science Letters*, 287(3–4), 412–419.
- Westerhold, T., Röhl, U., & Laskar, J. (2012). Time scale controversy: Accurate orbital calibration of the early Paleogene. *Geochemistry, Geophysics, Geosystems*, 13(6).
- Wu, L., Wilson, D. J., Wang, R., Yin, X., Chen, Z., Xiao, W., & Huang, M. (2020). Evaluating Zr/Rb ratio from XRF scanning as an indicator of grain-size variations of glaciomarine sediments in the Southern Ocean. *Geochemistry, Geophysics, Geosystems*, 21(11).
- Yamamoto, M., Suemune, R., & Oba, T. (2005). Equatorward shift of the subarctic boundary in the northwestern Pacific during the last deglaciation. *Geophysical Research Letters*, 32(5).
- Yamane, M. (2003). Late Quaternary variations in water mass in the Shatsky Rise area, northwest Pacific Ocean. *Marine Micropaleontology*, 48(3-4), 205-223.
- Yang, S., Ding, F., & Ding, Z. (2006). Pleistocene chemical weathering history of Asian arid and semi-arid regions recorded in loess deposits of China and Tajikistan. *Geochimica et Cosmochimica Acta*, 70(7), 1695-1709.
- Yin, Q. (2013). Insolation-induced mid-Brunhes transition in Southern Ocean ventilation and deep-ocean temperature. *Nature*, 494(7436), 222-225.
- Yin, Q. Z., & Berger, A. (2012). Individual contribution of insolation and CO<sub>2</sub> to the interglacial climates of the past 800,000 years. *Climate dynamics*, 38(3-4), 709-724.
- Yu, J., Gan, B., Jing, Z., & Wu, L. (2020). Winter Extreme Mixed Layer Depth South of the Kuroshio Extension. *Journal of Climate*, 33(24), 10419-10436.
- Zachos, J. C., Kroon, D., Blum, P., & Party, S. S. (2004). *Early Cenozoic extreme climates: the Walvis Ridge transect* (Vol. 208). College Station, TX (Ocean Drilling Program).
- Zhang, Y., Wallace, J. M., & Battisti, D. S. (1997). ENSO-like interdecadal variability: 1900–93. *Journal of climate*, 10(5), 1004-1020.
- Zhang, Z., Zhao, W., Qiu, B., & Tian, J. (2017). Anticyclonic eddy sheddings from Kuroshio loop and the accompanying cyclonic eddy in the northeastern South China Sea. *Journal of Physical Oceanography*, 47(6), 1243-1259.
- Zhao, W., Tarasov, P. E., Lozhkin, A. V., Anderson, P. M., Andreev, A. A., Korzun, J. A., ... & Wennrich, V. (2018). High- latitude vegetation and climate changes during the Mid- Pleistocene Transition inferred from a palynological record from Lake El'gygytgyn, NE Russian Arctic. *Boreas*, 47(1), 137-149.
- Zhong, Y., & Liu, Z. (2009). On the mechanism of Pacific multidecadal climate variability in

CCSM3: The role of the subpolar North Pacific Ocean. *Journal of physical oceanography*, 39(9), 2052-2076.

**Figure 1.** (a) Modern day sea surface temperature map of the northwest Pacific Ocean. Major currents discussed in the text are highlighted in black and labeled, and sites discussed in text are denoted by black dots outlined in white. (b) Cross section of the upper ocean (0–4000 m water depth) across the three sites denoted in panel A, across the Kuroshio Current Extension. Map and cross section created using Ocean Data View (Schlitzer, 2015) with sea surface temperature data from the World Ocean Atlas (Locarini et al., 2013).

**Figure 2.** Cluster Results Depth series developed for ODP Hole 1207A sediment core between 1330 0.0-30.0m. (a) Shipboard Graphic Lithology from ODP Leg 198. (b) Cluster Lithology displaying variability between Cluster 1 (blue) and Cluster 2 (red). (c) Elemental composition for cluster 1 (Clayey nannofossil ooze) and cluster 2 (Nannofossil ooze w/clay).

**Figure 3.** Power spectra and time-frequency analysis results for (a-b) benthic  $\delta^{18}\text{O}$  record (Ahn et al., 2017), (c-d) local insolation at  $37^\circ\text{N}$  in  $\text{W}/\text{m}^2$ , and (e-f) ODP Hole 1207A  $\ln \text{Ca}/\text{Ti}$  of normalized and standardized XRF data. Cumulative band power in the precession (0.04-0.06), obliquity (0.02-0.03), eccentricity (0.001-0.013) and heterodyne (0.0133-0.02) bands are highlighted in power spectra results (eccentricity = red, heterodynes = green, obliquity = blue, precession = grey). The MPT interval (highlighted in yellow) spans the interval in which there is the emergence of the eccentricity frequency in the benthic  $\delta^{18}\text{O}$  record of ice volume/deep ocean temperature until when the cumulative band power associated with eccentricity is greater than obliquity.

**Figure 4.** Depth series developed for ODP Hole 1207A between 0–30 mbsf and correlation to age-based time series data. Depth series data includes (a) shipboard graphic lithology column based on visual core description (Bralower et al., 2002); (b) cluster lithologies defined in this study using XRF core scanning data; (c) linear sedimentation rates (LSR) in  $\text{cm}/\text{kyr}$  determined from the age model used in this study (Table 1); (d) shipboard low-resolution physical property data of Natural Gamma Radiation (NGR) (light green), and porosity (black dashed line); (e) shipboard magnetic susceptibility (MS) (Bralower et al., 2002); (f) normalized and standardized XRF-based  $\ln \text{Zr}/\text{Sr}$  ratios; (g) shipboard color reflectance data  $L^*$ ; (h) normalized and standardized XRF-based  $\ln \text{Ca}/\text{Ti}$  ratios; Age-based times-series includes (i)  $\delta^{18}\text{O}$  benthic oxygen isotope stack (Ahn et al., 2017) with MISs labels for interglacial periods; (j,k, l) orbital parameters of obliquity (dark green), precession (light blue) and eccentricity (black), and insolation ( $37^\circ\text{N}$ ), respectively, as defined by Laskar et al. (2004); (m) astrochronology with correlation to Hole 1207A paleomagnetic normal (highlighted in grey) and reversed intervals (white background); (n) Local insolation at  $37^\circ\text{N}$  in  $\text{W}/\text{m}^2$ ; and (o) calcareous nannofossil datums with red dashed lines depicting tie points to depth series data. Summaries of depth series data as proxies for paleoenvironmental conditions are labeled below time series data. All XRF ratios are plotted with a 11-point running mean.

**Figure 5.** Elemental Ratio Depth Series for ODP Hole 1207A sediment core between 0.0 to 30.0 m. (a) XRF-based  $\ln \text{Zr/Sr}$ ; (b) XRF-based  $\ln \text{Ca/Ti}$ ; (c) cluster lithologies; (d) shipboard visual description lithologies. (e) foraminiferal benthic Stack  $\delta^{18}\text{O}$  from Ahn et al., 2017. (f) Magnetic polarity stratigraphy. Depth is further categorized into 3 interpreted zones; Pre-MPT glacial/interglacials (yellow), Post-MPT cooling (blue), and pronounced interglacials (red).

**Figure 6.** Normalized elemental counts from XRF core scanning at ODP Hole 1207A plotted against a global benthic foraminiferal  $\delta^{18}\text{O}$  stack (Ahn et al., 2017). Interglacial periods discussed in-text are denoted by MIS numbers. The wider vertical light gray bar indicates the periods encompassing MIS 15-9 and 29-25 when Zr, Ti, and Si counts decrease and Ca counts increase.

**Figure 7.** Correlation matrix of normalized elemental counts from XRF core scanning at ODP Hole 1207A. Pearson's correlation coefficients are displayed through positive values (red) and negative values (blue). Ellipses also display strength of correlations with more elliptical and darker colors reflecting stronger correlations. Shaded boxes represent statistically significant values (p-value <0.05) performed using a two-tailed test. Correlation analysis was performed using PAST 4.09 software (Hammer et al., 2001).

**Figure 8.** Age-based time series developed for ODP Hole 1207A between 0-2164 ka (0–30 mbsf). Time series data includes (a) cluster lithologies defined in this study using XRF core scanning data; (b) normalized and standardized XRF-based  $\ln \text{Ca/Ti}$  ratio; (c) normalized and standardized XRF-based  $\ln \text{Zr/Sr}$  ratio; (d) shipboard magnetic susceptibility (MS; brown dashed line) (Bralower et al., 2002); (e) sea surface temperatures (SSTs) from Subarctic North Pacific ODP Site 882; SSTs from eastern equatorial upwelling sites ODP Site 1020 (f) and 1012 (g); (h) Insolation representing seasonality (65°N; JJA-DJF); (i, j, k) orbital parameters of eccentricity (black), precession (light blue), and obliquity (dark green).  $\delta^{18}\text{O}$  benthic oxygen isotope stack (Ahn et al., 2017) with MISs labels for interglacial periods. Red shaded boxes denote periods encompassing MIS 15-9 and 29-25 where we interpret an expanded North Pacific Subtropical Gyre and pronounced warmth over Site 1207A.

**Table 1.** Principal Component Analysis results including eigenvalues, variance (%), and cumulative variance for Hole 1207A 0.0-30.0 mbsf. Bolded PC1-3 were used in hierarchical cluster analysis.

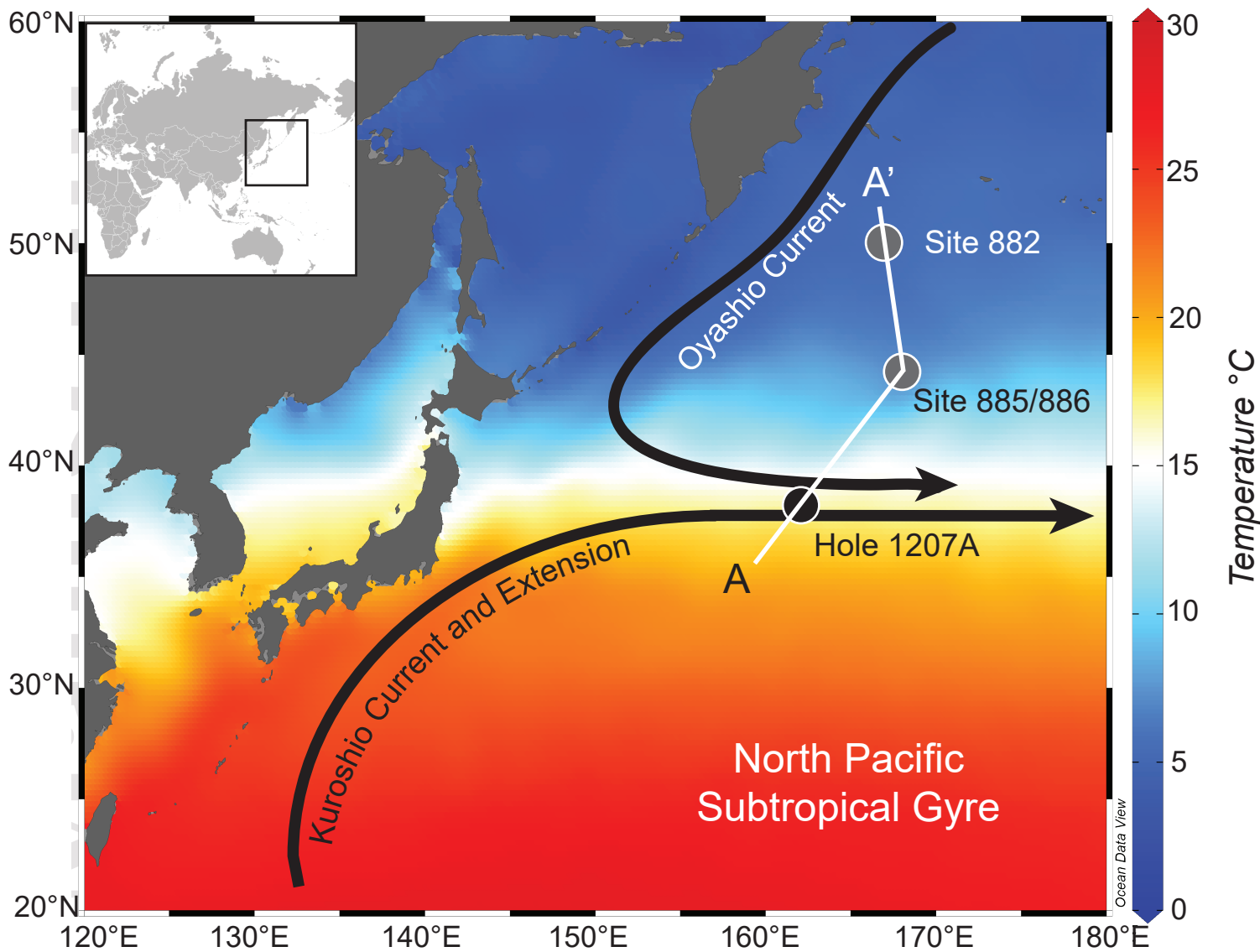
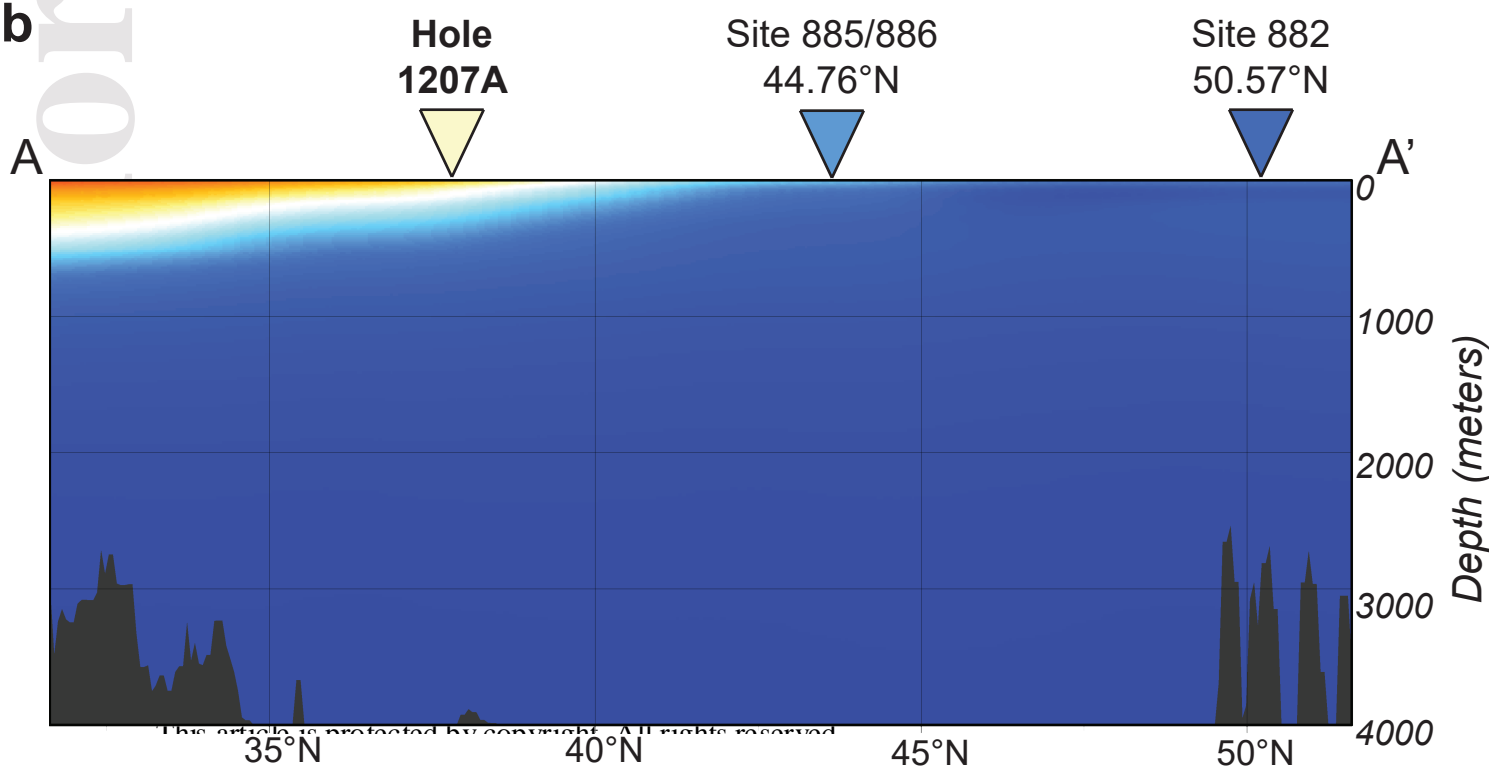
**Table 2.** Cluster lithology and elemental relationships. Shipboard facies and associated processes also defined.

**Table 3.** Age model used in this study based on magnetostratigraphy (Lam and Leckie, 2020b) and calcareous nannofossil biostratigraphy (Bralower et al., 2002) with ages of datums updated to those in Sutherland et al. (2019). T, top; B, bottom; FO, first occurrence; LO, last occurrence. The C1r.2n (Cobb Mountain) Chron was not identified during initial shipboard magnetostratigraphy and therefore was not used for this age model.

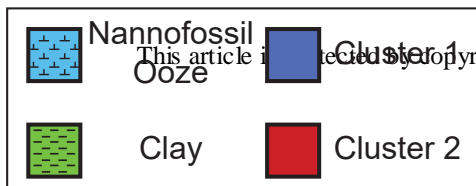
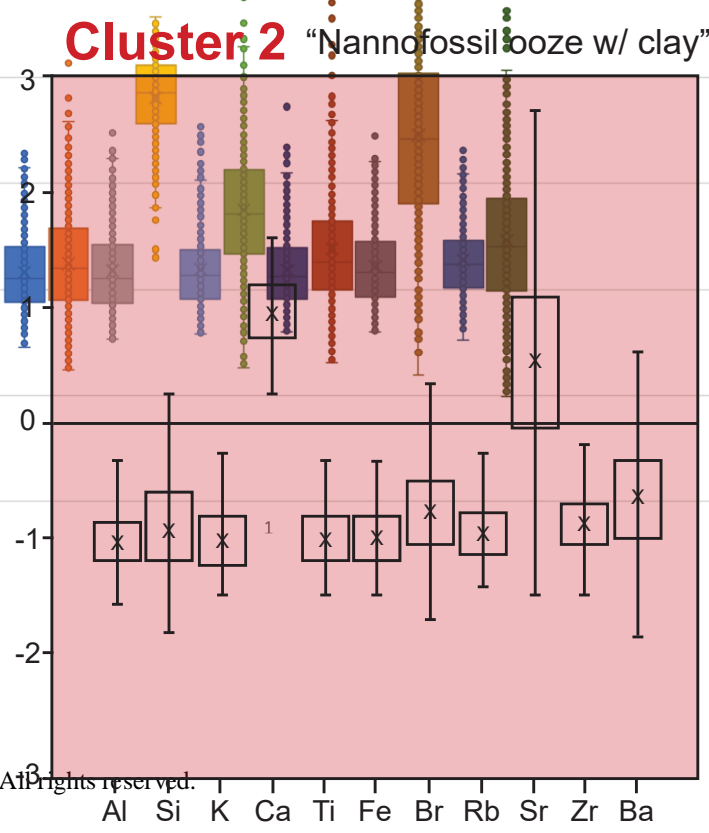
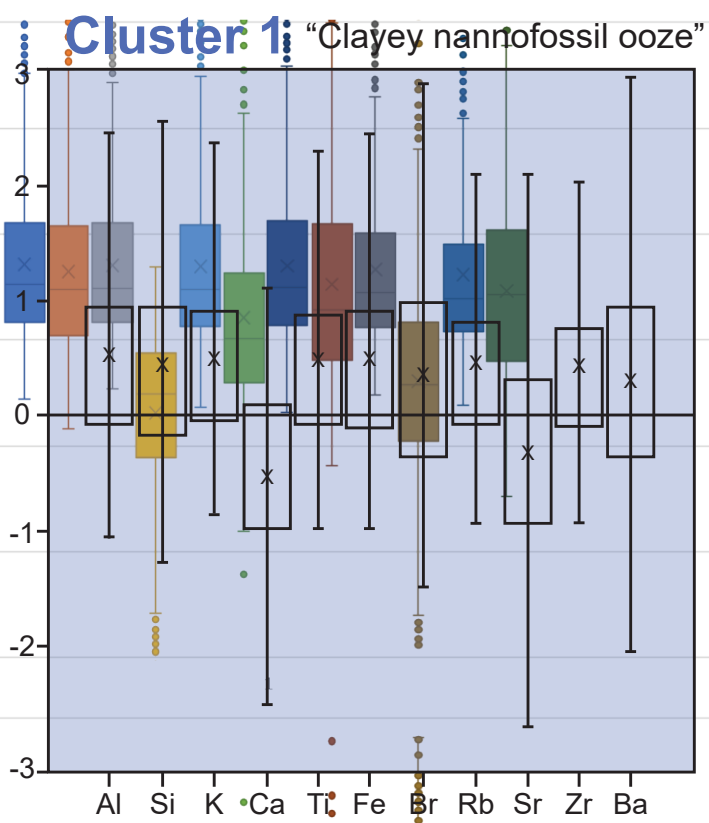
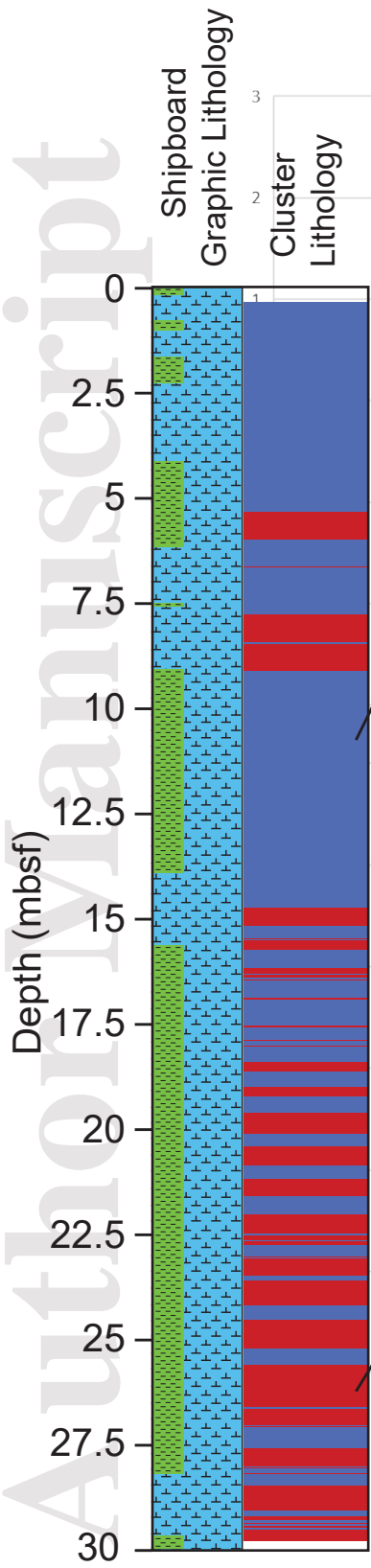
**Table 4.** Significant frequencies identified on the untuned XRF-based normalized and standardized values of  $\ln \text{Ca/Ti}$  with the associated orbital interpretations. The identification of orbital parameters in kyr is defined by their power association for 2164 ka to recent following the

Laskar et al., (2004) solution with 1 indicating greatest power and higher values indicating frequencies with subsequently less power (E1=95.7; E2=126.1; E3=54.4; O1=41.1, O2=28.9; O3=53.7; P1=19; P2=23.7; P3=22.4). Heterodyne frequencies and interpretations are bolded.

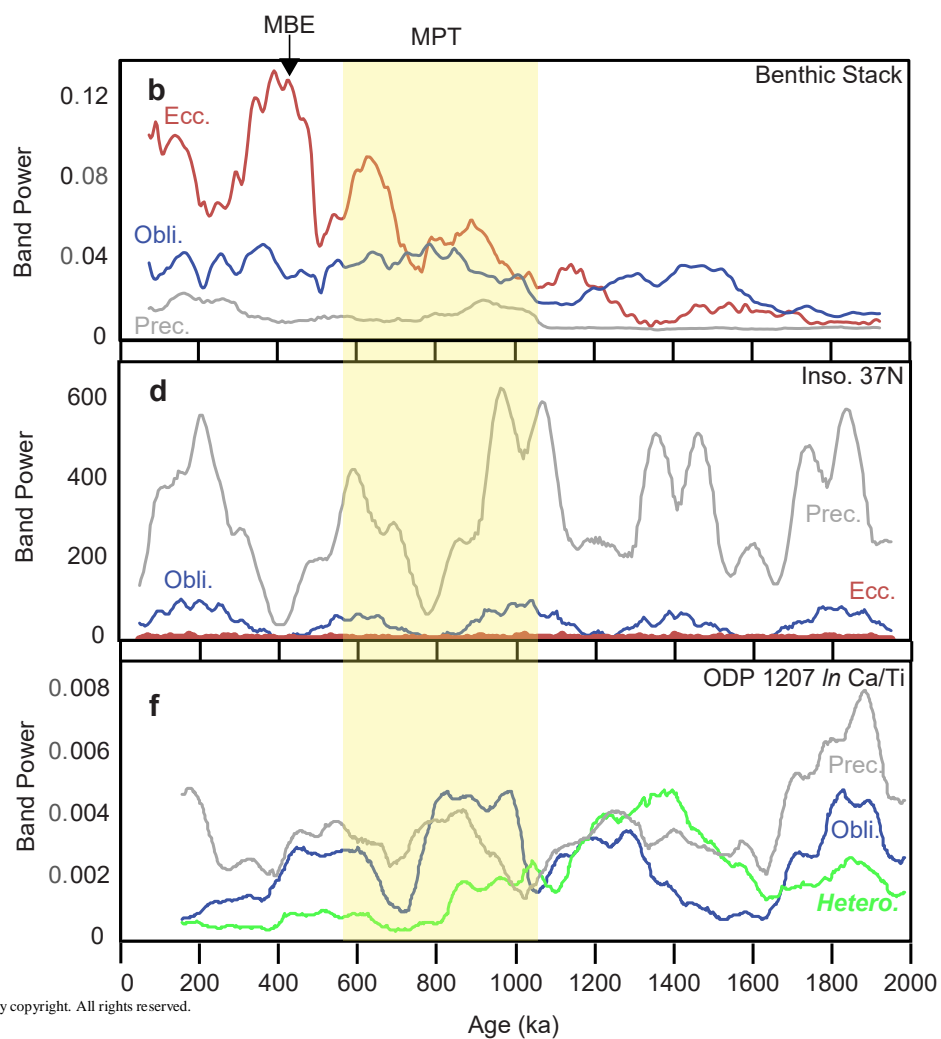
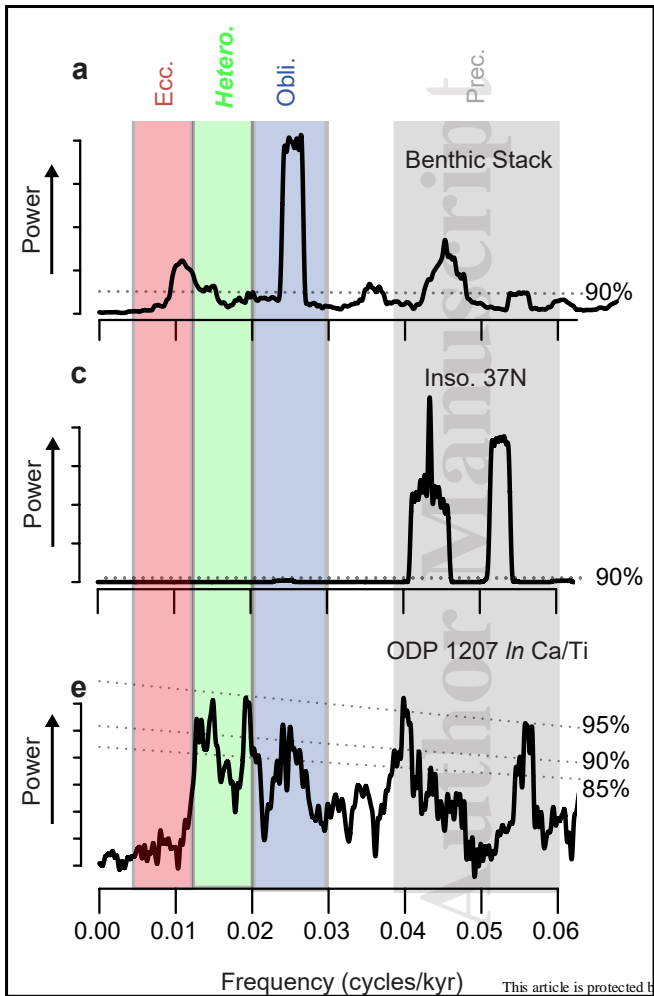
Author Manuscript

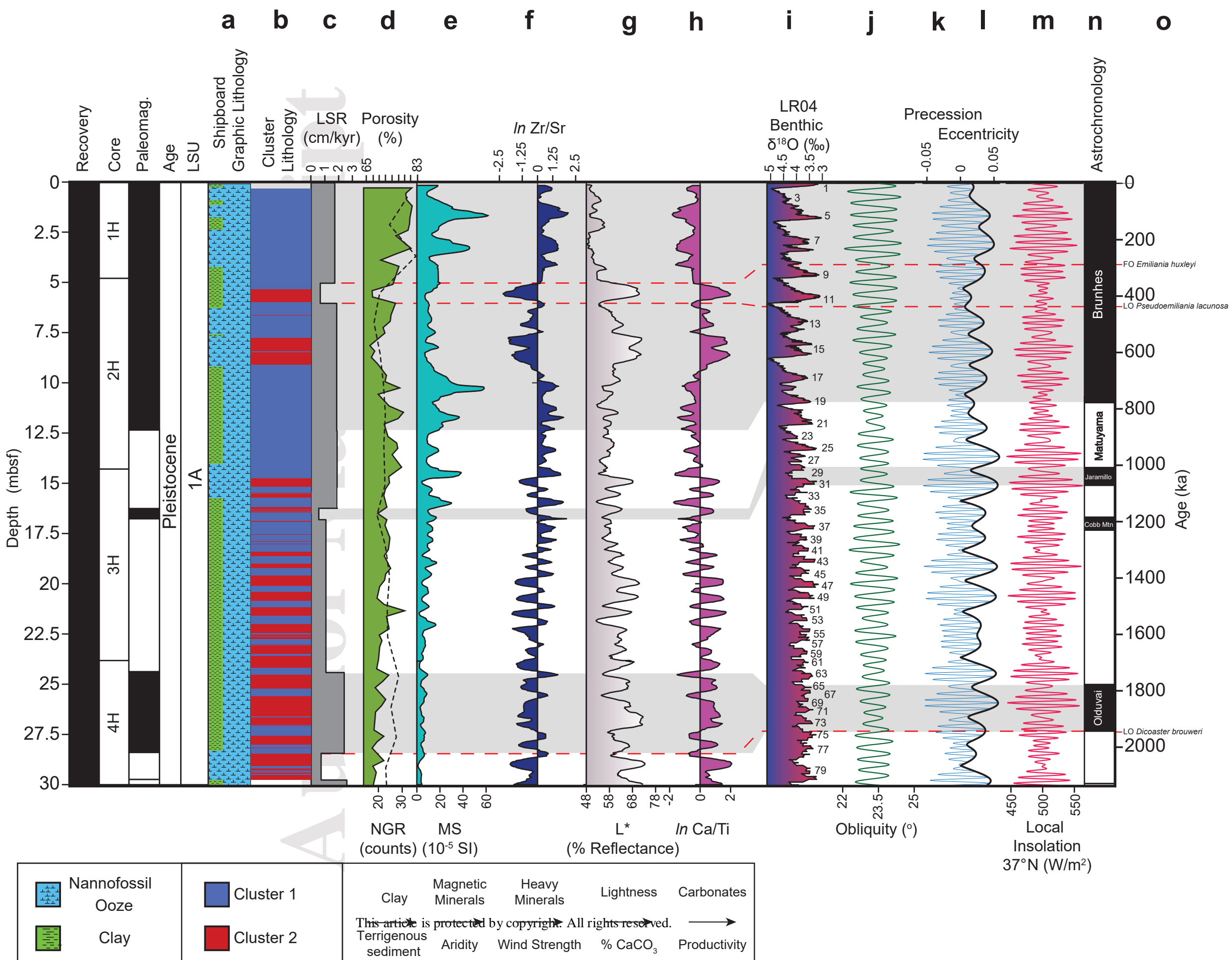
**a****b**

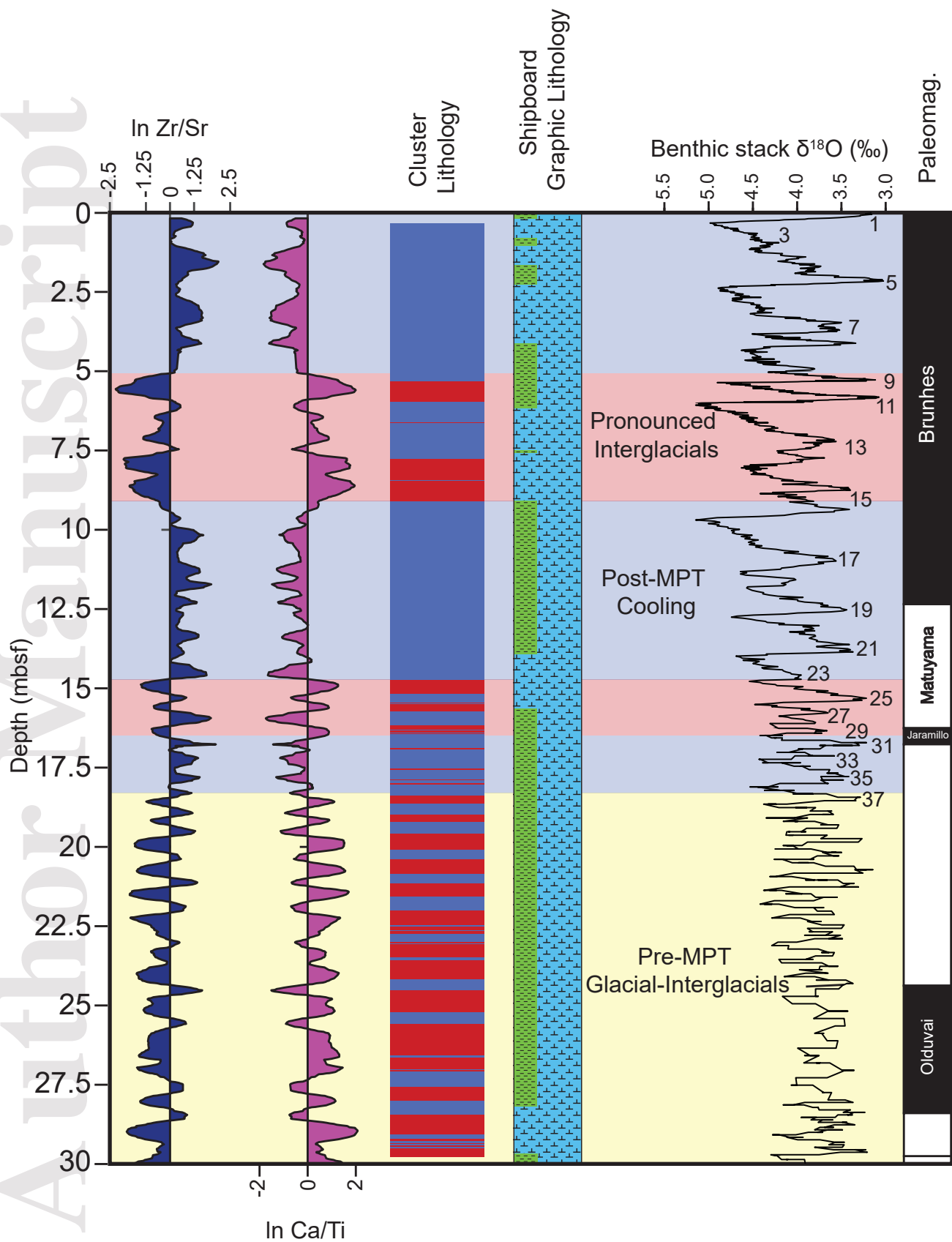


**a****b****c**

Author Manuscript





**a****b****c****d****e****f**

This article is protected by copyright. All rights reserved.

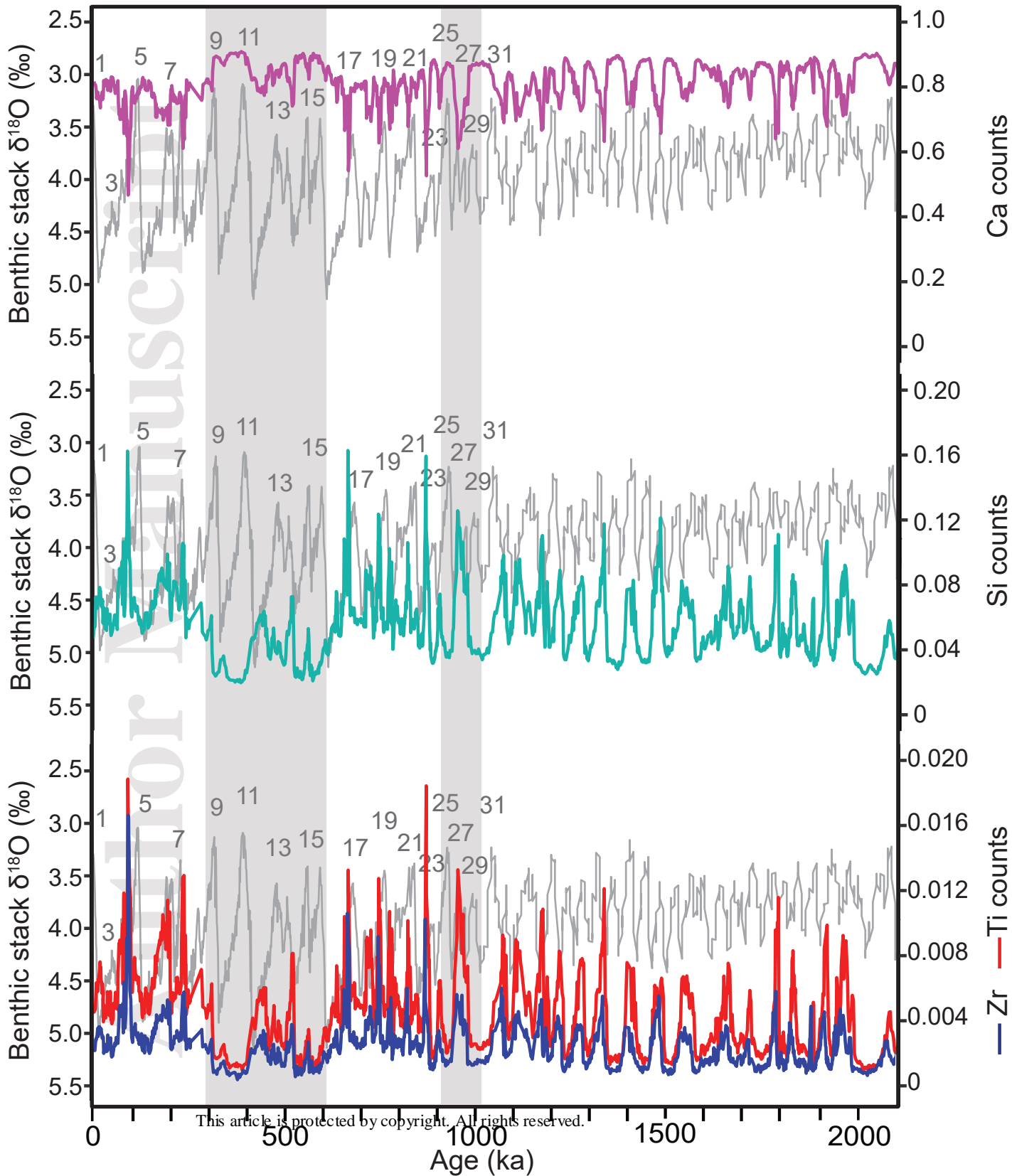
Wind Strength Carbonate Productivity

Cluster 1

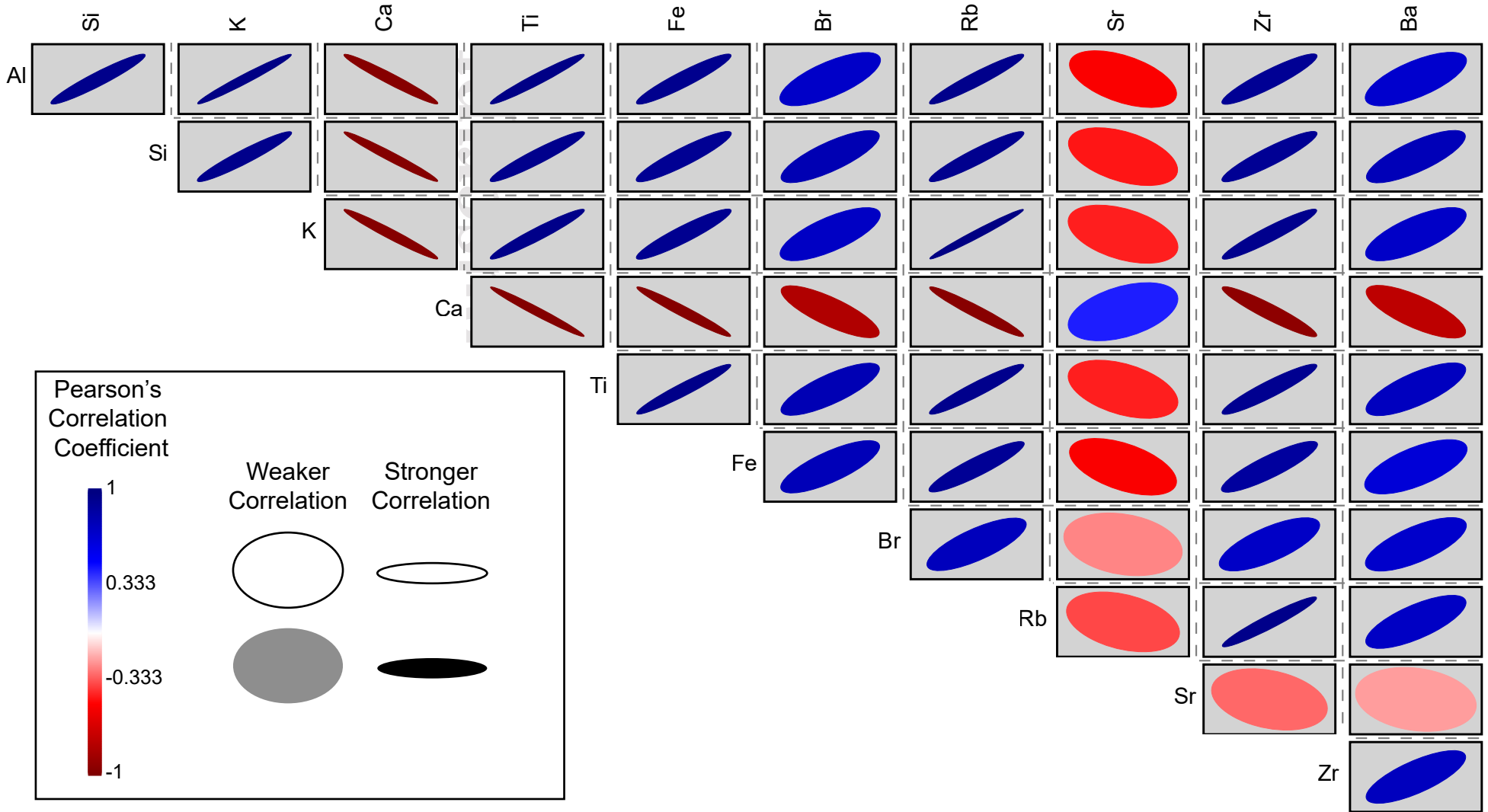
Cluster 2

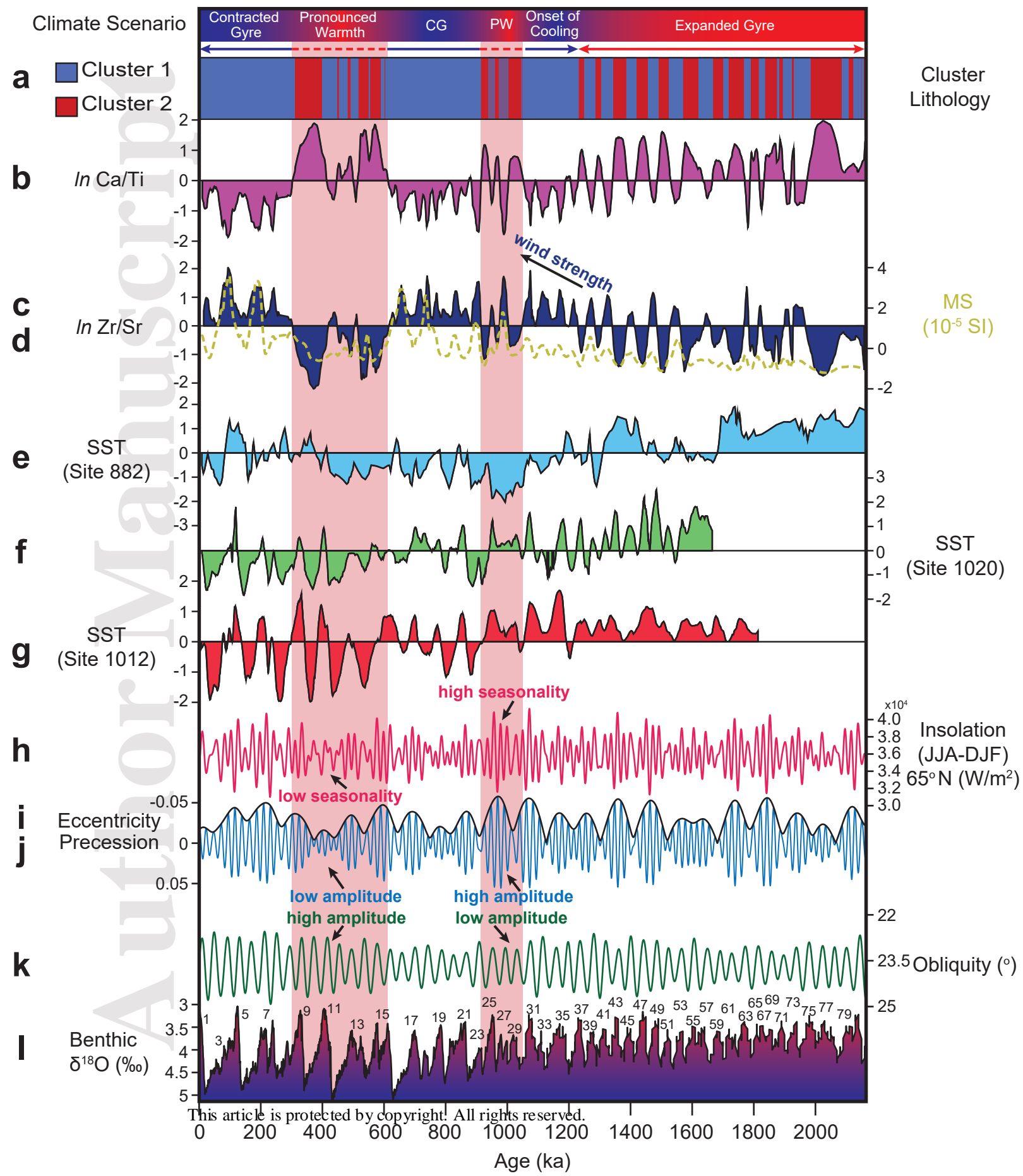
Nannofossil Ooze

Clay









| <b>PC</b> | <b>Eigenvalue</b>  | <b>Variance (%)</b> | <b>Cumulative Variance (%)</b> |
|-----------|--------------------|---------------------|--------------------------------|
| <b>1</b>  | <b>0.005025840</b> | <b>98.71</b>        | <b>98.71</b>                   |
| <b>2</b>  | <b>0.000045985</b> | <b>0.90</b>         | <b>99.62</b>                   |
| <b>3</b>  | <b>0.000010761</b> | <b>0.21</b>         | <b>99.83</b>                   |
| 4         | 0.000006233        | 0.12                | 99.95                          |
| 5         | 0.000001925        | 0.04                | 99.99                          |
| 6         | 0.000000313        | 0.01                | 99.99                          |
| 7         | 0.000000143        | 0.00                | 100.00                         |

| Cluster | Elemental Data  | Shipboard Facies                       | Processes   | Mode                         |
|---------|---|--|---|------------------------------|
| 1       | Positive value (+)<br>-Al, Si, K, Ti, Br, Zr, Ba, Fe, Rb<br>Negative value (-)<br>-Ca, Sr | Clayey nannofossil ooze (>25% clay)    | Low carbonate productivity and stronger winds, cold | Subtropical gyre contraction |
| 2       | Positive value (+)<br>-Ca, Sr<br>Negative value (-)<br>-Al, Si, K, Ti, Br, Zr, Ba, Fe, Rb | Nannofossil ooze with clay (<25% clay) | High carbonate productivity, weaker winds, warm     | Subtropical gyre expansion   |

| <b>Chron or Datum</b>             | <b>Depth (mbsf)</b> | <b>Age (ka)</b> | <b>Sedimentation Rate (cm/ka)</b> |
|-----------------------------------|---------------------|-----------------|-----------------------------------|
|                                   | 0.00                | 0               |                                   |
| FO <i>Emiliana huxleyi</i>        | 5.00                | 290             | 1.72                              |
| LO <i>Pseudoemiliana lacunosa</i> | 6.00                | 430             | 0.71                              |
| B C1n (Brunhes)                   | 12.35               | 773             | 1.85                              |
| B C1r.1r (Matuyama)               | 16.26               | 1008            | 1.66                              |
| B C1r.1n (Jaramillo)              | 16.77               | 1076            | 0.75                              |
| B C1r.3r                          | 24.38               | 1775            | 1.09                              |
| LO <i>Discoaster brouweri</i>     | 28.00               | 1930            | 2.34                              |
| B C2n (Olduvai)                   | 28.40               | 1934            | 10.00                             |
| B C2r.1n (Feni)                   | 29.73               | 2155            | 0.60                              |
| B C2r.2r (Matuyama continued)     | 43.13               | 2610            | 2.95                              |



| Frequency    | Period (kyr)  | Harmonic F-test Confidence Level | LOWSPEC Confidence Level Estimate | Interpretation                          |
|--------------|---------------|----------------------------------|-----------------------------------|---|
| <b>0.014</b> | <b>73.114</b> | <b>91.294</b>                    | <b>91.801</b>                     | <b>1/E1 – 1/O1 = 72.0 kyr</b>           |
| <b>0.016</b> | <b>61.887</b> | <b>92.181</b>                    | <b>81.793</b>                     | <b>1/E2 – 1/O1 = 61.0 kyr</b>           |
| <b>0.020</b> | <b>49.883</b> | <b>96.310</b>                    | <b>90.897</b>                     | <b>1/E2 – 1/E1 = 54.4 kyr</b><br>E3, O3 |
| <b>0.023</b> | <b>43.422</b> | <b>98.736</b>                    | <b>81.019</b>                     | <b>1/E4 – 1/O1 = 45.8 kyr</b>           |
| 0.026        | 38.401        | 94.851                           | 91.312                            | O1                                      |
| 0.041        | 24.475        | 96.783                           | 95.286                            | P2?                                     |
| 0.043        | 23.354        | 93.161                           | 74.522                            | P2                                      |
| 0.044        | 22.944        | 91.530                           | 79.133                            | P3                                      |
| 0.056        | 18.017        | 99.856                           | 94.602                            | P1                                      |